



RESEARCH ARTICLE

10.1029/2022JG007074

Key Points:

- Satellite-observed chlorophyll fluorescence showed a nonlinear wilting pattern in response to soil droughts on the Mongolian Plateau
- We modified the Soil-Canopy Observation of Photosynthesis and Energy fluxes (SCOPE) model and its ancillary radiative-transfer inversion algorithm to adequately evaluate dryland features
- The modifications enabled assessment of the physiological control of photosynthesis and retrieval of the wilting point of the study area

Supporting Information:

Supporting Information may be found in the online version of this article.

Correspondence to:

T. Kiyono,
kiyono.tomoki@nies.go.jp

Citation:

Kiyono, T., Noda, H. M., Kumagai, T., Oshio, H., Yoshida, Y., Matsunaga, T., & Hikosaka, K. (2023). Regional-scale wilting point estimation using satellite SIF, radiative-transfer inversion, and soil-vegetation-atmosphere transfer simulation: A grassland study. *Journal of Geophysical Research: Biogeosciences*, 128, e2022JG007074. <https://doi.org/10.1029/2022JG007074>






Received 3 JUL 2022

Accepted 3 APR 2023

© 2023. The Authors.

This is an open access article under the terms of the [Creative Commons Attribution-NonCommercial-NoDerivs License](https://creativecommons.org/licenses/by/4.0/), which permits use and distribution in any medium, provided the original work is properly cited, the use is non-commercial and no modifications or adaptations are made.

Regional-Scale Wilting Point Estimation Using Satellite SIF, Radiative-Transfer Inversion, and Soil-Vegetation-Atmosphere Transfer Simulation: A Grassland Study

T. Kiyono¹ , H. M. Noda¹, T. Kumagai² , H. Oshio³ , Y. Yoshida¹ , T. Matsunaga¹ , and K. Hikosaka⁴

¹Earth System Division, National Institute for Environmental Studies, Tsukuba, Japan, ²Graduate School of Agricultural and Life Sciences, The University of Tokyo, Tokyo, Japan, ³School of Environment and Society, Tokyo Institute of Technology, Yokohama, Japan, ⁴Graduate School of Life Sciences, Tohoku University, Sendai, Japan

Abstract Although water availability strongly controls gross primary production (GPP), the impact of soil moisture content (SMC) (wilting point) is poorly quantified on regional and global scales. In this study, we used 10 years of observations of solar-induced chlorophyll fluorescence (SIF) from the Greenhouse gases Observing Satellite (GOSAT) satellite to estimate the wilting point of a semiarid grassland on the Mongolian Plateau. Radiative-transfer model inversion and soil-vegetation-atmosphere transfer simulation were sequentially conducted to distinguish the drought impacts on plant physiology from the changes in the leaf-canopy optical properties. We modified an existing inversion algorithm and the widely used Soil-Canopy Observation of Photosynthesis and Energy fluxes model to adequately evaluate dryland features, for example, sparse canopy and strong convection. The modified model, with retrieved parameters and calibration to GOSAT SIF, predicted realistic GPP values. We found that (a) the SIF yield estimated from GOSAT showed a clear sigmoidal pattern in relation to drought, and the estimated wilting point matched ground-based observations in the literature within $\sim 0.01 \text{ m}^3 \text{ m}^{-3}$ for the SMC, (b) tuning the maximum carboxylation rate improved the SIF prediction after considering the changes in the leaf-canopy optical properties, implying that GOSAT detected drought stress in leaf-level photosynthesis, and (c) the surface energy balance significantly impacted the grassland's SIF; the modified model reproduced observed SIF well (mean bias = $0.004 \text{ mW m}^{-2} \text{ nm}^{-1} \text{ sr}^{-1}$ in summer), whereas the original model predicted substantially low values under weak horizontal wind conditions. Some model-observation mismatches in the SIF suggest that more research is needed for fluorescence parametrization (e.g., photoinhibition) and for additional observation constraints.

Plain Language Summary Solar-induced chlorophyll fluorescence, a weak radiation emitted as a byproduct of photosynthesis, can potentially be used to assess plant physiological status, which is especially promising for evaluating poorly quantified soil drought (wilting) impacts on the carbon cycle. However, the potential of satellite-observed fluorescence to improve wilting prediction by vegetation models has not been sufficiently explored because of the confounding effects of plant physiological stress and visible damage (i.e., leaf browning and defoliation). In this study, we distinguished physiological wilting from visible damage by estimating leaf pigment contents and leaf amounts from satellite-observed reflectance with the aid of a radiative transfer model and a state-of-the-art vegetation model. We found that some model modifications were necessary to adequately evaluate the dryland features, for example, sparse vegetation cover and thermally induced atmospheric flow. The observed fluorescence showed a clear nonlinear response to the soil moisture content, which is characteristic of wilting. The model-based analysis suggested that the nonlinear response resulted from physiological stress, and the estimated wilting point matched the ground-based observations in the literature well. Since our approach is based on biophysics and satellite data, our findings and methods should help in understanding and predicting terrestrial water and carbon cycles in other regions.

1. Introduction

Drought is a critical hazard for human society and ecosystems. For example, the recent rapid warming and long-lasting drought over the Mongolian Plateau has reduced water resources (e.g., Brutsaert & Sugita, 2008), caused land degradation and frequent dust storms (Lee & Sohn, 2011) and enhanced the risk of livestock mortality by reducing pasture production (Nandintsetseg et al., 2018). Since gross primary production (GPP) is fundamental

and changes in advance of other biological processes, monitoring and modeling the impacts of drought on GPP have received great attention (e.g., Fisher et al., 2020; J. Huang et al., 2017; A. Verhoef & Egea, 2014).

Soil drought reduces the GPP and transpiration ($\text{CO}_2/\text{H}_2\text{O}$ exchange rate) mainly through three physiological processes: (a) stomatal closure by hydraulic limitation (Sperry & Love, 2015), (b) stomatal closure by chemical signals (abscisic acid) (Tardieu et al., 2015), and (c) reductions in the mesophyll conductance of CO_2 diffusion, most likely by reducing the membrane permeability (aquaporin) (Flexas et al., 2012). From a macroscopic/geophysical viewpoint, these processes are parametrized as reductions in stomatal conductance and/or the maximum photosynthesis rate. For both variables, the drought effects are expressed frequently using a piecewise linear function (A. Verhoef & Egea, 2014) because the soil moisture content (SMC) does not affect gas exchange under well-watered conditions. The key parameters are two apparent thresholds, the SMC value (or its corresponding intensive variable, water potential) at which the gas exchange rate starts to decrease and at which the exchange stops (the latter is the so-called permanent wilting point). To avoid complexity, hydrologists and climate modelers tend to use the SMC for parametrization (e.g., Bonan, 2015; Hornberger et al., 2014; A. Verhoef & Egea, 2014). Here, we use the term “wilting point” to refer to the pair of SMC thresholds; these two thresholds do not have strict physical meaning but are regression coefficients, so they cannot be determined independently. Note that different parameters are sometimes used, for example, the value at half maximum, but the methods presented in this paper do not depend on the specific form of the equation.

Satellite remote sensing has played a pivotal role in quantifying terrestrial carbon and water cycles. However, satellite-based diagnostic GPP products, most of which depend on the Moderate Resolution Imaging Spectroradiometer (MODIS), often fail to track dryland interannual dynamics (Biederman et al., 2017; Stocker et al., 2019). This error may result from insufficient parametrization of the wilting point, which is frequently neglected in diagnostic GPP products. Introducing the wilting effect to the diagnosis potentially reduces estimates of GPP by 10%–19% globally and increases the interannual variability by more than 100% across one-fourth of vegetated lands (Stocker et al., 2019). The nonlinear feature of the wilting point is also poorly constrained in prognostic models (Rogers et al., 2017), and it is a major driver of carbon cycle uncertainty between the earth system models (ESMs) investigated in the CMIP5 model intercomparison project (Trugman et al., 2018).

Spaceborne observations of solar-induced chlorophyll fluorescence (SIF) have attracted attention since its first global measurement by the Greenhouse gases Observing Satellite (GOSAT) launched in 2009 (Frankenberg & Berry, 2018). SIF is a weak radiation emitted as a byproduct of photosynthesis, and satellites often observe SIF reductions associated with drought (Jonard et al., 2020). However, it is widely known that leaf chlorophyll content significantly changes SIF but not GPP (e.g., Koffi et al., 2015), and furthermore, recent theoretical studies suggest nonnegligible impacts of other leaf chemical compounds such as brown pigments and the soil on the reabsorption of SIF in the canopy, that is, the escape probability (Cui et al., 2020; Liu et al., 2019; van der Tol et al., 2019; Verrelst et al., 2015). Since prolonged drought induces defoliation or reduces chlorophyll content and increases brown leaves, it is necessary to distinguish the SIF changes that are very weakly linked with GPP (e.g., chlorophyll contents, escape probability) from the GPP-linked SIF signals (e.g., stomatal closure, carboxylation capacity reductions). Physical soil-leaf-canopy radiative-transfer model inversion (e.g., W. Verhoef et al., 2018; Weiss & Baret, 2016) enables the estimation of leaf and soil optical property changes, and state-of-the-art vegetation models such as the Soil-Canopy Observation of Photosynthesis and Energy fluxes (SCOPE) model (van der Tol et al., 2009; Yang et al., 2021) enable the prediction of optical property impacts on SIF. Mechanistic links are essential for understanding processes beyond mere correlations and for utilizing SIF with prognostic models.

In this study, we attempted to estimate the wilting point (the two SMC thresholds mentioned above) of a semi-arid grassland from satellite SIF, combined with observed spectral reflectance and radiative-transfer inversion. Furthermore, we modified the widely used SCOPE model to demonstrate how wilting signals detected by satellite SIF constrain grassland GPP through soil-vegetation-atmosphere transfer (SVAT) simulation. It is notable that previous dry grassland studies reported underestimation in SCOPE SIF; Verma et al. (2017) found underestimations when comparing the SCOPE model to the OCO-2 satellite, and Pacheco-Labrador et al. (2019) reported that the model reproduced tower-observed SIF and GPP with overestimations in the leaf area index (LAI) and the canopy temperature, which implies an exaggeration of heat stress in the model. Our modifications to the SCOPE model were mainly improvements of the model's capability to reproduce observed SIF under wet conditions, which is a prerequisite for unbiased model parametrization based on wilting signals. We also modified the inversion algorithm to utilize satellite SIF products with relatively large footprints (GOSAT as an example) for sparse vegetation in drylands.

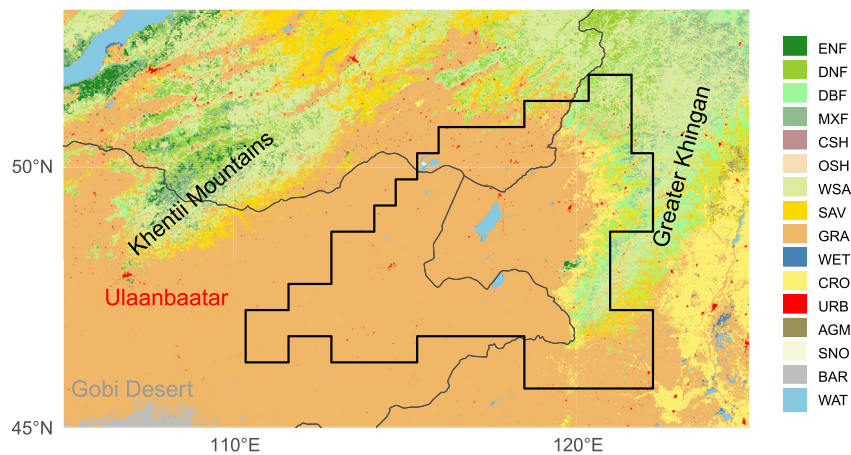


Figure 1. International Geosphere-Biosphere Programme land cover map of the study area for 2015. Abbreviations represent evergreen needleleaf forests (ENF), deciduous needleleaf forests (DNF), deciduous broadleaf forests (DBF), mixed forests (MXF), closed shrublands (CSH), open shrublands (OSH), woody savannas (WSA), savannas (SAV), grasslands (GRA), wetlands (WET), croplands (CRO), urban areas (URB), agricultural mosaics (AGM), snow and ice (SNO), barren areas (BAR), and water bodies (WAT).

2. Study Area and Climate

The study area is the eastern end of the Mongolian Plateau (46–52°N; 110–122°E; elevation 700–1,000 m), which has experienced rapid warming and drought since the late 1990s (Xu et al., 2015). Figure 1 illustrates the land cover map, according to the International Geosphere-Biosphere Programme (IGBP) (Friedl & Sulla-Menashe, 2019). The typical plant species are cool-season C3 grasses (Y. Yan et al., 2018).

According to the Modern-Era Retrospective Analysis for Research and Applications, Version 2 (MERRA-2) reanalysis product (Gelaro et al., 2017), the annual precipitation is approximately 400 mm, and the maximum and minimum values of the 2-m air temperature are 35°C and –35°C, respectively. The study area boundary was determined by a hierarchical cluster analysis (Badr et al., 2015) using the monthly means of the MERRA-2 air temperature, precipitation, vapor pressure deficit, and the top-of-canopy (TOC) irradiance of photosynthetically active radiation (PAR) during 2009–2018. Since SMC products generally have large uncertainty (H. Li et al., 2021) and the MERRA-2 SMC is not assimilated with observational data, the reliability was confirmed by comparison with other data sets (Gruber et al., 2019; Martens et al., 2017) (Text S1 and Figure S1 in Supporting Information S1). We found that the MERRA-2 SMC is better than or as good as the other products.

3. Strategies of Inverse and Forward Simulations

Figure 2 overviews the model calibration procedure. Radiative-transfer model inversion and SVAT simulation were sequentially conducted to distinguish the drought impacts on physiology from changes in leaf-canopy optical properties. We adopted basically the same parameter optimization procedure as that used in van der Tol et al. (2016). First, the leaf-canopy optical properties were retrieved using Bayesian optimization to address the ill-posedness of the inversion. Then, the physiological parameters were determined by minimizing errors in SIF predictions using the ordinary least-squares method.

3.1. Inverting the RTMo Soil-Leaf-Canopy Radiative-Transfer Model

3.1.1. Overview and Modifications

We carried out inversion analysis to retrieve the canopy structural, leaf optical, and soil parameters of the grassland. The optical radiative transfer model (RTMo) is a submodule of the SCOPE model. It is composed of the

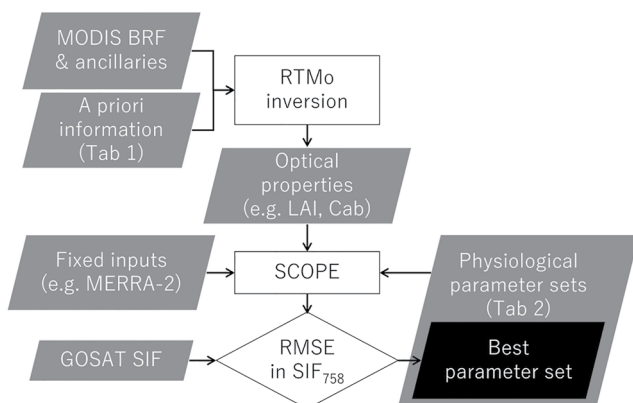


Figure 2. Schematic diagram of the model calibration procedure.

PROSPECT leaf model (Jacquemoud & Baret, 1990), the 4SAIL canopy model (W. Verhoef, 1998), and the BSM soil model (Yang et al., 2020). The inversion algorithm based on RTMo (van der Tol et al., 2016; W. Verhoef et al., 2018) enables retrieval of the parameters from TOC spectral reflectance (400–2,400 nm). We used the RTMo retrieval code version itc2020 with the Optipar2017_ProspectD library. This library was also used in the forward simulation. The RTMo parameters were retrieved from the MODIS bidirectional reflectance factor (BRF) (Lyapustin & Wang, 2018) by convolving with its spectral response function.

We have modified the RTMo retrieval code as follows.

1. While the original code retrieves the parameters from the TOC hemispherical-directional reflectance factor or top-of-atmosphere radiance, we modified it to enable retrieval from TOC BRF to use the MODIS BRF data.
2. The original code assumes a horizontally homogeneous canopy, which is generally invalid at the >1-km scale, especially for sparse vegetation in drylands. Therefore, we introduced fractional vegetation cover (FVC) as a new canopy structural parameter to adjust surface heterogeneity. Linear spectral mixing of vegetated and nonvegetated lands was assumed as in the studies using the SAIL model at large scales, including those for the global LAI products provided by the European Space Agency (Baret et al., 2007; Fuster et al., 2020; Weiss & Baret, 2016; Weiss et al., 2007).
3. We implemented procedures to calculate model parameter errors (Rodgers, 2000) used in the optimization process in the Bayesian inversion to avoid overfitting to observed reflectance and improve retrieval robustness (detailed in Text S2 in Supporting Information S1).

3.1.2. Retrieval Procedure

The cost function χ^2 of the RTMo retrieval is based on a Bayesian inversion approach,

$$\chi^2 = \sum_{i=1}^n \left(\frac{R_i^{\text{obs}} - R_i^{\text{mod}}(\mathbf{x})}{\sigma_{\epsilon,i}} \right)^2 + \sum_{j=1}^m \left(\frac{x_j - \mu_j}{\sigma_{a,j}} \right)^2, \quad (1)$$

where R_i is the reflectance in the i th bands of a spectroradiometer (MODIS BRF here, $n = 12$); superscripts designate observation (obs) and RTMo (mod). σ_{ϵ} denotes the root-sum-square of instrumental noise and model uncertainty (Equation S1 in Supporting Information S1). $\boldsymbol{\mu}$ denotes the a priori values, and \mathbf{x} denotes the RTMo parameters to be retrieved. The uncertainty (i.e., standard deviation) σ_a of the a priori values was set to the default or quantified by assuming uniform probability distributions as in W. Verhoef et al. (2018) (but based on the strict definition here; $\sigma_a^2 = \int_{\text{LB}}^{\text{UB}} \frac{(x-\mu)^2}{\text{UB-LB}} dx$). Table 1 and Table S1 in Supporting Information S1 summarize the settings. Minimization of the cost function (Equation 1 and Equation S1 in Supporting Information S1) was iteratively solved using the trust-region-reflective method. The posterior uncertainty $\sigma_p = [\sigma_{p,1}, \sigma_{p,2}, \dots, \sigma_{p,m}]^T$ can be expressed as

$$[\sigma_{p,1}^2, \sigma_{p,2}^2, \dots, \sigma_{p,m}^2]^T = \text{diag} \left[(\mathbf{K}^T \mathbf{S}_{\epsilon}^{-1} \mathbf{K} + \mathbf{S}_a^{-1})^{-1} \right], \quad (2)$$

where \mathbf{S}_{ϵ} and \mathbf{S}_a are the (diagonal) covariance matrices of the measurement error and the a priori uncertainty, respectively (the diagonals are $\sigma_{\epsilon,i}^2$ and $\sigma_{a,j}^2$, respectively), and $\mathbf{K} = \partial \mathbf{R} / \partial \mathbf{x}$ is the Jacobian matrix. The values of σ_p depend on the assumptions in \mathbf{S}_a but provide insights into which retrievals are more strongly constrained by observation.

The optical properties can be retrieved with a radiative-transfer model only when the relationship between the observed radiometric quantity and the parameter of interest is consistent and unique, typically when partial derivatives of spectral radiance/reflectance with respect to the parameters, or Jacobians, are linearly independent. Therefore, the number of retrievable parameters depends on the spectral range and resolution of an instrument, and the Jacobians help identify the parameters that can be retrieved and the need for a priori information. For example, van der Tol et al. (2016) used RTMo and analyzed the Jacobians for a typical crop with a known soil reflectance, assuming a hyperspectral sensor (1-nm resolution in 400–900 nm). However, to date, there has been no RTMo (or PROSAIL) retrieval study for MODIS considering unknown soil reflectance and FVC, so we address it as follows.

Figure 3 shows the simulated BRF and Jacobians for a typical summer day at the spectral resolution of MODIS. The RTMo retrieval was applied to the averaged BRF within a GOSAT footprint of 10.5 km diameter. The right

Table 1
Retrieval Settings for Vegetation Parameter Estimation

	Definition	Unit	μ	σ_a	LB	UB
B	Soil brightness	(-)	0.45	0.26	0	0.9
BSMlat	Dry soil spectral shape	(-)	28 ^a	4 ^a	-	-
BSMlon		(-)	56 ^a	4 ^a	-	-
SMC	Volumetric water content in surface soil	(vol%)	MERRA-2	5 ^b	-	-
Cab	Chlorophyll <i>a + b</i> content	($\mu\text{g cm}^{-2}$)	15 ^c	45	0	100
Cca	Carotenoid content	($\mu\text{g cm}^{-2}$)	$f(\text{Cab})^d$	4	0	25
Cant	Anthocyanin content	($\mu\text{g cm}^{-2}$)	0	1	-	-
Cdm	Dry matter content	(g cm^{-2})	0.005	0.008	0	0.02
Cw	Equivalent water thickness	(cm)	0.01	0.02	0	0.05
Cs	Brown pigments content	(-)	0.1	1.4	0	2.5 ^e
N	Leaf structure parameter	(-)	1.4	1	-	-
LAI	Leaf area index	($\text{m}^2 \text{m}^{-2}$)	MCD15 C6	^f	0	7
LIDFa	Average leaf inclination	(-)	-0.5 ^g	0.76	-	-
LIDFb	Bimodality of the leaf angle distribution	(-)	-0.5 ^g	0.76	-	-
FVC	Fractional vegetation cover	($\text{m}^2 \text{m}^{-2}$)	MOD44 C6	0.1 ^h	0	1

Note. μ is the a priori mean, σ_a is the a priori standard deviation, and LB and UB are the lower and upper boundaries, respectively. The retrieved parameters in the vegetation parameter estimation step are shown in bold face.

^aTable S1 in Supporting Information S1. ^bReichle et al. (2017). ^cMinimum value of green leaves defined by Weiss and Baret (2016). ^dThe regression line from Sims and Gamon (2002, Figure 7). ^ePacheco-Labrador et al. (2021). ^f $\max(1/3, \text{standard deviation of MCD15 LAI})$. 1/3 is based on the 3σ rule and the difference between MCD15 LAI and observed total LAI (K. Yan et al., 2016). ^gPlagio-erectophile with 65° average leaf inclination (W. Verhoef, 1998). ^hClimatological mean of the standard deviation of the MOD44 FVC in the study area.

panels show the spectrum of the Jacobian matrix for the same datum and show clear implications. (a) It is obvious that the dominant parameter is *LAI*, and the other parameters for the structure of the canopy or leaf (*LIDF*, *FVC*, and *N*) have similar spectral shapes, suggesting the difficulty of retrieving these parameters simultaneously. (b) The sensitivity to *SMC* is weak, and its spectral shape is similar to that of soil brightness (*B*) except for the signs. (c) The first- and second-peak positions of the brown pigments *Cs* overlap with the peaks of the soil parameter *BSMlat* and chlorophyll content *Cab*, respectively. Therefore, (a) we included the a priori *LAI* and *FVC* using

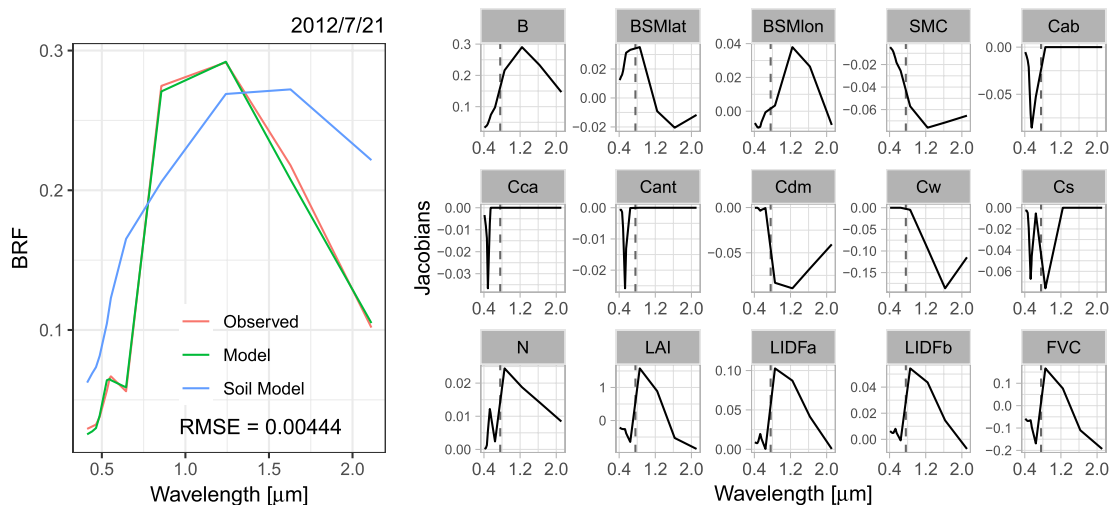


Figure 3. (left) Observed and simulated bidirectional reflectance factor (BRF) spectra for Moderate Resolution Imaging Spectroradiometer bands 1–12 on a typical summer day (leaf area index = $1.9 \text{ m}^2 \text{m}^{-2}$, $\text{Cab} = 23 \mu\text{g cm}^{-2}$). (right) The corresponding Jacobians ($\partial\text{BRF}/\partial x$) for each model parameter x . Dashed lines in the right panels indicate the position of the Greenhouse gases Observing Satellite solar-induced chlorophyll fluorescence retrieval window (758 nm).

MODIS products (MCD15A2H, Myneni et al., 2015; MOD44B, Dimiceli et al., 2015) to constrain these parameters and fix the other structural parameters, (b) we fixed the *SMC* value to that of MERRA-2, and (c) we adopted a 2-step retrieval strategy. First, for preparation, *BSMlat* and *BSMlon* values were retrieved using only summer data with homogeneous green cover ($LAI > 1$ and $FVC > 0.75$) by assuming $Cs = 0$. Then, we retrieved vegetation properties with fixed values of *BSMlat* and *BSMlon* obtained in the first step. The uncertainty in unretrieved parameters was explicitly considered using Equation S1 in Supporting Information S1 in both steps. The root mean square error (RMSE) of the modeled spectrum in Figure 3 (left), obtained by these procedures, was 0.004; this is comparable to previous studies that used high-resolution images (e.g., Bayat et al., 2018).

3.2. Modifications to the SCOPE Soil-Vegetation-Atmosphere Transfer Model

3.2.1. Overview and Bug Fixing

The multilayer SVAT model SCOPE can predict spectral and directional radiative transfer, including the emissions of SIF (van der Tol et al., 2019) and thermal infrared radiation. We used the latest version, SCOPE2.1. This model has two options for the photosynthesis-fluorescence scheme, TB12 and MD12, and we used the latter because of its more process-based nature (Mohammed et al., 2014). The MD12 scheme is composed of the photosynthesis model of Farquhar et al. (1980) and the MD12 quantum yield parametrization (Dayyoub, 2011) as follows:

$$\Phi_F = \min[\Phi_F^{PQ}, \Phi_F^{NPQ}], \quad (3)$$

$$\Phi_F^{NPQ} = \Phi_P \frac{k_F}{k_{PSII}} \frac{1}{q_{Ls} - J_a/J_{max}}, \quad (4)$$

where Φ_F and Φ_P are quantum yields of fluorescence (superscripts designate photochemical [PQ] and nonphotochemical quenching [NPQ]) and photochemistry, respectively. Under moderate- to high-light conditions expected at satellite overpass times, plants are generally in the “NPQ-phase” (Magney et al., 2020). k is the rate constant (fluorescence (F) and the intrinsic (i.e., fully open and functional) rate of photosystem II (PSII)), the values of which were adopted from Thum et al. (2017). q_{Ls} is the fraction of the functional reaction center (=0.95 in this study), J_{max} is the maximum electron transport rate, and J_a is the actual electron transport rate under colimitation with the carboxylation rate. Φ_P is a function of J_a and the PAR absorbed by chlorophylls, and the values of J_a and J_{max} are predicted by the photosynthesis model; the J_{max} value at 25°C was determined from the maximum carboxylation rate V_{cmax} using the empirical relationship derived by Leuning (1997). Additional details are provided in Thum et al. (2017).

We found several issues in SCOPE2.1 that can lead to significant errors in drylands (Text S3 in Supporting Information S1). Notably, the density of air ρ_a is fixed to 1.2047 kg m⁻³ (i.e., dry air at 20°C and 101 kPa). This is simple but significant in regions at high altitudes and a nontemperate climate (e.g., the Mongolian Plateau); this results in a large bias in the leaf temperature because sensible and latent heat fluxes are proportional to ρ_a . The impact is shown in the Section 5.

After fixing the issues, we further modified SCOPE2.1 to adequately evaluate GPP and SIF signals in semiarid grasslands. We present an outline of the modified code below. Table 2 summarizes the parameter settings, including the newly implemented settings.

3.2.2. Introducing the Drought Stress Function

Wilting reduces the mesophyll conductance of CO₂ diffusion, which apparently (temporary) reduces V_{cmax} (Zhou et al., 2013). Because SCOPE2.1 does not predict this phenomenon, we expressed it by multiplying a piecewise-linear function by V_{cmax} (hereafter, V_{cmax} denotes the values under wet conditions),

$$V_{cmax,app} = V_{cmax} \cdot \max\left[\min\left[\frac{\theta - \theta_w}{\theta_c - \theta_w}, 1\right], 0\right]. \quad (5)$$

The predictions of the SCOPE model, such as the surface energy balance and the values of GPP and SIF, were calculated using the apparent value $V_{cmax,app}$. Here, θ is the volumetric water content of the rhizosphere, and we assumed it is identical to the MERRA-2 surface *SMC* (θ_{scm}) and *SMC* in RTMo. The wilting-point parameters θ_c

Table 2
Primary Parameter Settings in SVAT Simulation

	Definition and unit	Value or range {from, to, step}	References
Aerodynamics and canopy geometry			
d	Zero-plane displacement height (m)	~0.4 in summer ^a	MERRA-2
z_o	Roughness length for momentum (m)	$f(d, LAI)^b$	CLM5
h_c	Canopy height (m)	$f(d, LAI)^b$	"
l_w	Leaf characteristic length (m)	0.04	"
CO₂/H₂O exchange			
V_{cmax}	Maximum carboxylation rate at 25°C (μmol m ⁻² s ⁻¹)	{20, 80, 20}	Rogers (2014)
k_v	Decaying coefficient for vertical V_{cmax} distribution (–)	$f(V_{cmax})^c$	CLM5
T_{year}	Growth temperature (Kattge & Knorr, 2007) (°C)	30	
g_{1M}	Medlyn slope parameter (kPa ^{1/2})	{4.61, 5.89, 0.64} ^d	CABLE and CLM5
g_0	Minimum stomatal conductance (mol (H ₂ O) m ⁻² s ⁻¹)	0.01	
θ_c	SMC at which $V_{cmax,app}$ starts to decrease (vol%)	{14, 18, 1}	
θ_w	SMC at which $V_{cmax,app}$ becomes zero (vol%)	{8, 14, 2}	
Fluorescence			
f_{qe}	Fluorescence yield at dark-adopted conditions (–)	0.012 ^e	JSBACH
q_{Ls}	Fraction of functional reaction centers (–)	0.95 ^f	Porcar-Castell (2011)
k_{NPQs}	Rate constant of sustained NPQ (–)	0	"
Soil			
I	Thermal inertia (J m ⁻² s ^{-1/2} K ⁻¹)	620	Bennett et al. (2008)
θ_{sat}	Porosity (vol%)	45.3	Montzka et al. (2017)
Ψ_{sat}	Air entry hydraulic head (cm)	9.9 ^g	"
b	Clapp-Hornberger parameter (–)	1.92 ^g	"

Note. Newly added variables from SCOPE2.1 are shown in bold face. Search ranges for the values of V_{cmax} , g_{1M} , θ_c , and θ_w are shown in brackets.

^aNot assimilated, from GEOS-5. ^bEquations 5.125–127 of Lawrence et al. (2020). ^cLloyd et al. (2010). ^dThe 95% confidence interval range for C3 grassland from De Kauwe et al. (2015, Table 1). ^eThum et al. (2017). ^fThe value in summer, most unstressed conditions in Porcar-Castell (2011). ^gConverted from the values of van Genuchten parameters in the study area using the relationship proposed by Rawls et al. (1992).

and θ_w are linked with the soil–plant hydraulic system properties, but we used Equation 5 for brevity; note that the SCOPE model has no hydrological module. We assumed that SMC affects SIF through J_a and Φ_p (Equations 3 and 4) but does not affect J_{max} since Equation 5 was used to express mesophyll diffusion. This nonstomatal limitation parametrization is in line with the observed weak relationship between SIF and stomatal closure (see the commentary by Magney et al., 2020).

In addition, we replaced the Ball-Berry stomatal conductance model used in SCOPE2.1 with the model of Medlyn et al. (2011) because the relative humidity-based Ball-Berry model is too sensitive to atmospheric aridity (see e.g., Paschalis et al., 2017).

3.2.3. Replacing the Aerodynamic Resistance and Soil Evaporation Schemes

We also replaced the aerodynamic resistance and soil evaporation schemes used in SCOPE2.1 with those used in the Community Land Model version 5 (CLM5) (Lawrence et al., 2020) for the following reasons.

- The aerodynamic resistance scheme used in SCOPE (Wallece & Verhoef, 2000) assumes local eddy diffusion and neglects large-eddy mixing in the convective boundary layer. This approach overestimates the aerodynamic resistance and canopy temperature for the short vegetation grown in regions where strong convection occurs (i.e., dryland grasses). This error is avoided in the CLM5 scheme by considering the large eddy effects through a parametrization using the Deardorff velocity (Stull, 1988). In addition, SCOPE2.1 neglects the leaf boundary layer (Text S3 in Supporting Information S1) and furthermore does not predict the boundary layer resistance for the soil surface, which brings another bias and high dependency on site-specific calibration.

- Although a parametrization of soil surface resistance for evaporation (vapor diffusion in soil pore space) is implemented in SCOPE2.1, we could not find documentation and validation. The experimental conditions (e.g., soil depth) are not documented in the model description papers (van der Tol et al., 2009; Yang et al., 2020), the source code (calc_rsrbs.m) and the manual (<https://scope-model.readthedocs.io/en/master/>). Furthermore, we found a substantial difference between predictions by the parametrization used in SCOPE and that used in the major models (Text S4 and Figure S2 in Supporting Information S1). The built-in parametrization only depends on the SMC and does not consider physical fundamentals such as the soil porosity and temperature, while the dry surface layer model used in CLM5 considers all these fundamentals.

Since both SCOPE and CLM5 explicitly calculate the energy balance of the soil surface, we were able to introduce these schemes in a manner compatible with CLM5. See Chapter 5 of the CLM5 documentation (Lawrence et al., 2020) for details. However, the surface soil thickness in CLM5 (2 cm) does not agree with that in MERRA-2 (5 cm). This disagreement potentially affects predictions of SIF and GPP by changing the canopy temperature through the sensible heat and thermal radiation fluxes from the soil surface. To evaluate this impact, we conducted a simulation using the 2-cm SMC obtained from the JRA-55 reanalysis (Kobayashi et al., 2015) and compared it to the result based on the MERRA-2 SMC (Text S1 and Figure S3 in Supporting Information S1). We found nonnegligible differences in the time soon after rain but in general, the impacts on GPP and SIF were almost negligible (<3% difference in 97% of the cases in the study period).

4. Data Processing

4.1. GOSAT SIF

We used the SIF data from GOSAT obtained during 2009–2018. The relatively long record and high accuracy of GOSAT SIF, which has been previously verified (Doughty et al., 2022; Oshio et al., 2019), are preferable for evaluating dryland interannual dynamics. The data processing used here was basically the same as in Oshio et al. (2019), but the data-filtering thresholds were modified as described in Text S5 in Supporting Information S1. We used the L1B product, radiance data, version V201.202 of the Thermal And Near infrared Sensor for carbon Observation—Fourier Transform Spectrometer (TANSO-FTS) onboard GOSAT and retrieved SIF from a spectral window of 756.0–759.1 nm using the spectral fitting method (Frankenberg & Berry, 2018). Since the location of GOSAT observational points depends on the period, we selected the observations with 100% grassland in the IGBP land cover and <15% woodland cover in MOD44B. Approximately 20–60 observations per month were obtained after filtering and screening.

To interpret the observed SIF radiance F ($\text{W m}^{-2} \text{nm}^{-1} \text{sr}^{-1}$) at a retrieval wavelength λ (~ 758 nm here), an expression analogous to Monteith's light-use efficiency model is frequently adopted (Frankenberg & Berry, 2018):

$$\pi F(\lambda) = I_{\text{PAR}} \cdot f_{\text{PAR}} \cdot \epsilon_{\text{F}}(\lambda) \cdot f_{\text{esc}}(\lambda), \quad (6)$$

where I_{PAR} is the TOC irradiance in the PAR, f_{PAR} is the fraction of the PAR absorbed by green leaves, ϵ_{F} is the SIF-emission efficiency ($\propto \Phi_{\text{F}}$), and f_{esc} is the fraction of SIF escaping from the canopy. The SIF yield ($=\epsilon_{\text{F}} \cdot f_{\text{esc}}/\pi$) is commonly used to remove the contribution of APAR ($=I_{\text{PAR}} \cdot f_{\text{PAR}}$). The corresponding APAR value to the GOSAT SIF was obtained from the MODIS f_{PAR} (MCD15A2H, averaged within each GOSAT footprint) and the MERRA-2 I_{PAR} ($0.5^\circ \text{ lat} \times 0.625^\circ \text{ lon}$) at 13:30 local time (LT) (the overpass time of GOSAT) of the same day as the GOSAT observations.

4.2. Experimental Setups and SIF-Based Calibration of the SCOPE Model

Three experiments were conducted to demonstrate model improvement. The control (CTRL) run was based on the modified SCOPE model with $V_{\text{cmax}} = 60 \mu\text{mol m}^{-2} \text{s}^{-1}$, the Medlyn slope parameter $g_{\text{IM}} = 5.25 \text{ kPa}^{1/2}$ (typical values for C3 grass; Table 2), and the well-watered assumption. The “SCOPE2.1” run was based on the original code with almost the same parameter values as the CTRL run; the Ball-Berry slope g_{IB} was set to 9 (unitless). The ZEXP run is a virtual “zero thermal expansion” simulation; the settings are the same as the CTRL run except convection was turned off (both the Monin-Obukhov stability correction and convective boundary layer mixing), and $\rho_{\text{a}} = 1.2047 \text{ kg m}^{-3}$ was fixed as the original code.

The benefit of constraining SIF for GPP estimation was tested using the modified model. Four physiological parameters (V_{cmax} , θ_{c} , θ_{w} , and g_{IM}) were calibrated by minimizing the RMSE of SCOPE SIF from GOSAT SIF

through a grid search. The search ranges of parameters were determined based on the settings for C3 grasslands in ESMs (Table 2). First, V_{cmax} and g_{1M} values were calibrated using wet data ($\theta_{5\text{cm}} > 19$ vol%). Calibration was separately conducted for June–August (JJA) and the remainder of the year to distinguish drought impacts from phenology. The run using the best parameter set was named the calibrated (CAL) run.

4.3. Forcing and Benchmarking Data Sets

The modified and original SCOPE models were forced by MERRA-2 meteorology at the 10-m height and the atmospheric CO₂ concentration at the surface-pressure level obtained from the GOSAT L4B product version V02.07. The spectral shape of the TOC irradiance was fixed to the default (FLEX-S3_std.atm), and broadband MERRA-2 irradiance data were used to scale the magnitude; the direct and diffuse components were separately scaled by making a minor modification to the code. Continuous 16-hr simulations during the daytime were conducted for each GOSAT observation because accurate ground heat flux calculations require a soil temperature history (Bennett et al., 2008). We used the retrieved RTMo parameters but replaced the uncertain C_{ab} data ($\sigma_p > 20 \mu\text{g cm}^{-2}$) with its monthly mean value.

Although there was a grassland flux tower site in Mongolia (AsiaFlux KBU site; S.-G. Li et al., 2005), it was closed in the launch year of GOSAT, so field data were unavailable. Instead, the performance of the models was evaluated by comparison with the MERRA-2 latent heat flux of evapotranspiration (IE_{total}), the MODIS land surface temperature (LST) (MYD11A1, Wan et al., 2015), and three diagnostic GPP data sets (MYD17A2H, Running et al., 2015; VPM, Zhang et al., 2017; a machine-learning model based on FLUXNET2015, Zeng et al., 2020), which have an 8- or 10-day resolution. MYD17 and VPM are light-use efficiency models based on MODIS reflectance; MYD17 is calibrated to process-based models, while VPM is calibrated to field observations. We did not use the MOD17 GPP because of a concern about sensor degradation in Terra/MODIS (Lyapustin et al., 2014) and because a small uncertainty in the gap-filling process was expected in our study area, which was mostly under clear sky conditions. Since the study area has sparse vegetation, we adopted a “mosaic” approach; a total surface flux was evaluated as a weighted sum of the fluxes from vegetated and nonvegetated surfaces weighted by FVC.

It is notable that the interannual variations in MERRA-2 IE_{total} are derived from an assimilation of meteorological observations because MERRA-2 LAI was fixed to the monthly climatology in 1982–1998 (Reichle et al., 2017). The sensible and latent heat fluxes are modified to match the observed air temperature and humidity. This top-down constraint is strong enough to retrieve the land surface processes (see Wei et al., 2013, e.g.). Therefore, the agreement in interannual variations in IE_{total} between MERRA-2 and our reflectance- and SIF-based approach can be considered a quasiobservational indicator for model performance. Figure S4 in Supporting Information S1 provides proof of concept in our study area. As expected, MERRA-2 showed interannual variations in IE_{total} that were more strongly correlated with the MODIS LAI ($r = 0.93$) than the MERRA-2 LAI ($r = 0.82$), which suggests significant observation contributions.

5. Results

5.1. Observed Seasonal and Interannual Dynamics

Figure 4 shows the 10-year time series of MERRA-2 meteorology and satellite data (MODIS LAI and FVC, and GOSAT SIF). The monthly means of the cloud fraction (CF) within the field of view of the GOSAT FTS were <20% in general (Figure 4d), and the monthly means of SIF₇₅₈ approached zero in winter, almost within the margin of the 90% confidence interval (CI), except in February 2010 and 2015. These results supported data consistency and quality during the growing season.

The monthly means of the 2-m air temperature fall below 0°C for approximately half of the years, and most precipitation falls during short periods in summer (Figure 4a). The precipitation showed large interannual variations, and the SMC decreased in early summer in 2011, 2016, 2017, and 2018 when precipitation was delayed (Figure 4b). On a monthly basis, the precipitation was strongly correlated with the MODIS LAI ($r = 0.90$), and the LAI was strongly correlated with the SIF ($r = 0.76$). However, even when the LAI did not decrease, the SIF dropped below $0.15 \text{ mW m}^{-2} \text{ nm}^{-1} \text{ sr}^{-1}$ when the mean SMC among GOSAT footprints fell below ~15–16 vol%, for example, in August 2010, June 2013, July 2016, and July 2017.

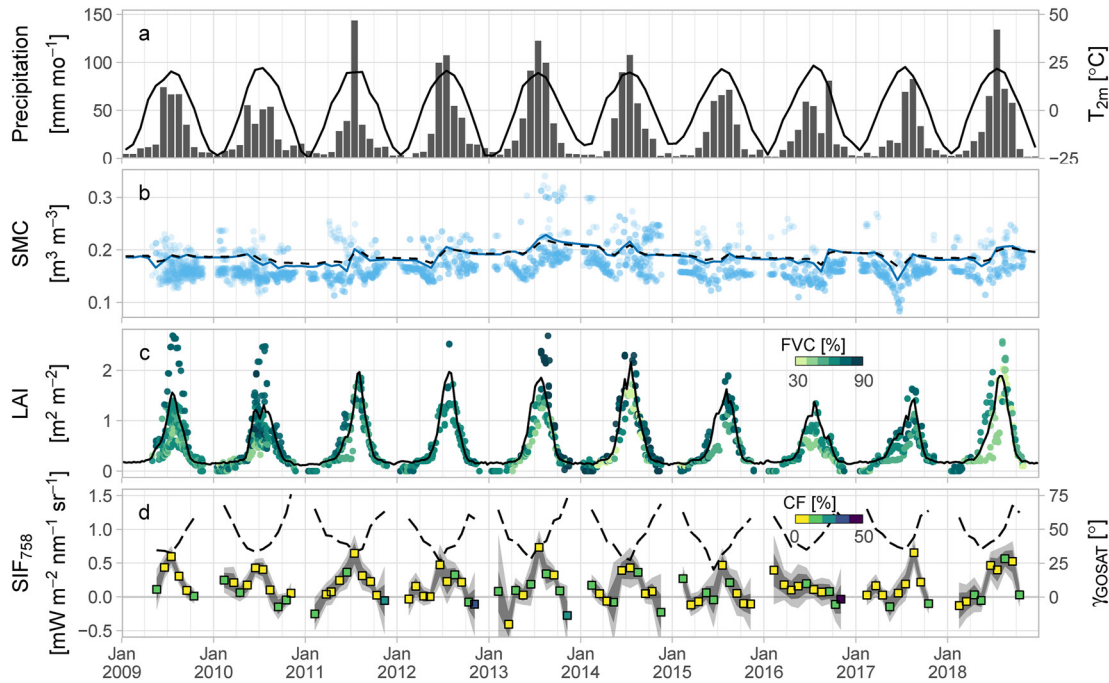


Figure 4. (a, b) Time series of MERRA-2 meteorology and (c) Moderate Resolution Imaging Spectroradiometer leaf area index and fractional vegetation cover, representing the mean quantities within each Greenhouse gases Observing Satellite (GOSAT) footprint (circles) and within the grassland in the study area boundary (bars and lines): precipitation (bars in a), monthly mean air temperature T_{2m} (line in a), and predawn soil moisture content at depths of 0–5 cm (blue symbols in b) and 10–100 cm (dashed line in b). (d) Monthly means of GOSAT SIF_{758} (squares) and ancillary data: dark and light shades indicate the standard error and the 90% confidence interval of the SIF, respectively; colors in squares indicate the cloud fraction (CF) in the field of view; and dashed lines indicate the phase angle γ_{GOSAT} .

There is no clear relationship between the SIF values and the phase angle γ_{GOSAT} (i.e., hot spot). However, this does not mean surface homogeneity, as seen by large variations in the MODIS FVC values (Figure 4c); the FVC values dropped below 50% frequently in 2014 and 2018.

5.2. Inversion Results and Justification of the Forward Model

Among the three modifications to the RTMo retrieval code, the introduction of FVC had the largest impacts on retrievals. When FVC was neglected (i.e., $FVC = 1$ is fixed), this bias was compensated by underestimation in LAI and Cab (see the Jacobian in Figure 3), and the values of Cab dropped below $10 \mu\text{g cm}^{-2}$ in most cases (Figure S5 in Supporting Information S1).

Figure 5 shows the inversion results using the modified RTMo retrieval code. The RMSE in the modeled BRDF increased in winter (not shown) and ranged from 0.0025 to 0.0287. The retrieved values of LAI and FVC are higher than those of the a priori MODIS products in general (Figures 5a and 5b); the increase in LAI was remarkable in low- LAI cases. The LAI results were expected since the MODIS algorithm retrieves green LAI (K. Yan et al., 2016), whereas RTMo retrieves the total LAI , including brown leaves. All the retrieved LAI values fall within the range of $\pm 1 \text{ m}^2 \text{ m}^{-2}$ from the priors. Figures 5c and 5d show the time series of the retrieved chlorophyll content Cab and brown pigments Cs , respectively (see Figure S6 in Supporting Information S1 for Cw and Cdm). They exhibit clear seasonality, and the Cab values reach $20\text{--}40 \mu\text{g cm}^{-2}$ in summer and do not clearly decrease in the drought years of 2015–2017. In general, the retrieved Cs shows the opposite phase to that of Cab .

Using these 10-year retrievals, the f_{esc} at 758 nm was predicted by the SCOPE model (Figure 6). The f_{esc} decreased from 0.55 to 0.2 with the increase in Cs , which strongly absorbs 758-nm SIF (Figure 3). Higher LAI (i.e., fewer canopy gaps) increases the canopy interception of photons, but the relationship between LAI and f_{esc} was not clear in the grassland.

Figure 7a shows the evapotranspiration difference between the modified and original models. The SCOPE2.1 run substantially overestimated IE_{total} compared with MERRA-2 ($r = 0.60$, mean bias = $+129 \text{ W m}^{-2}$), while

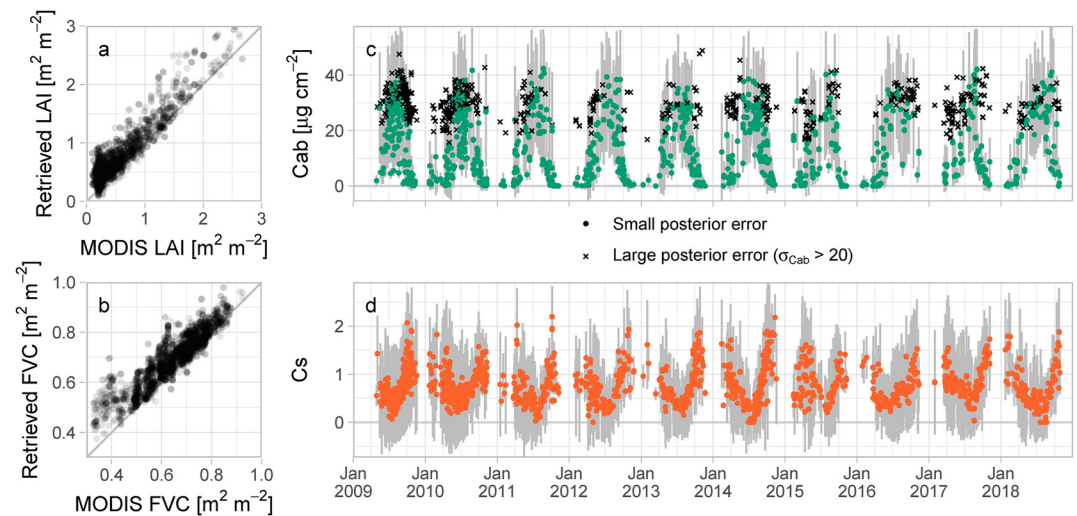


Figure 5. (a, b) Comparison between the a priori (Moderate Resolution Imaging Spectroradiometer products) and the a posteriori values for leaf area index and fractional vegetation cover. (c, d) Time series of the retrieved chlorophyll content Cab and brown pigments Cs . Error bars indicate the standard deviation of the a posteriori values.

the CTRL run tracked it better ($r = 0.85$, mean bias = $+30 \text{ W m}^{-2}$). The higher IE_{total} and lower correlation with MERRA-2 in the SCOPE2.1 run resulted from the high soil evaporation rate caused by the small soil surface resistance (Text S2 and Figures S2 and S7 in Supporting Information S1). Figures 7c and 7d show diurnal changes in the simulated SIF_{758} and canopy average temperature $T_{c,ave}$ on a calm summer day (23 July 2010). The CTRL run predicted a monotonic peak in SIF_{758} , whereas the SCOPE2.1 and ZEXP runs predicted clear midday depression. At the time of the GOSAT overpass (13:30 LT), the SIF_{758} value in the CTRL run reached 250% of the prediction by SCOPE2.1. This substantial difference results from the canopy temperature; the peak value of $T_{c,ave}$ around noon was $\sim 35^\circ\text{C}$ in the CTRL run, whereas it reached $\sim 50^\circ\text{C}$ in the other two runs. Some of these differences are caused by aerodynamic resistance, as shown in Figure 7b. The above-canopy aerodynamic resistance in SCOPE2.1 (gray circles) steeply increased when the 10-m horizontal wind speed dropped below 2 m s^{-1} , whereas the CTRL run predicted more stable changes. The predicted SIF values in the SCOPE2.1 and ZEXP runs differed despite their similar $T_{c,ave}$ values, which resulted from three heat-related physiological differences. Namely, there are two issues in the original implementation of the photosynthesis model in MD12 (Text S3 in Supporting Information S1) and the difference in humidity sensitivity between the Ball-Berry and Medlyn models.

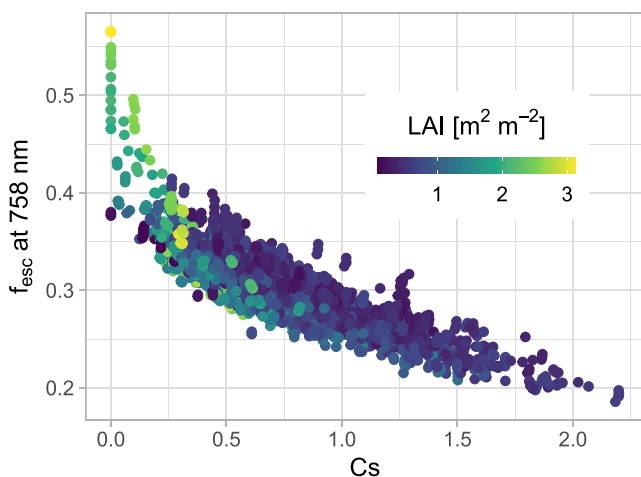


Figure 6. Simulated escape ratio f_{esc} at 758 nm for Greenhouse gases Observing Satellite observations throughout the study period and the relationships to retrieved Cs and leaf area index.

5.3. Drought Impacts on SIF and GPP

Both Figures 8a and 8b show the relationships between GOSAT SIF and SMC, considering APAR as a controlled variable. The SIF increased with APAR, while its slope (=SIF yield) increased with θ_{5cm} (Figure 8a); the threshold of $\theta_{5cm} = 15.4 \text{ vol}\%$ resulted in the largest difference between the SIF yields obtained under dry- and wet-SMC conditions. The mean \pm standard error ($10^{-6} \text{ nm}^{-1} \text{ sr}^{-1}$) of the SIF yields were 2.78 ± 0.14 (wet) and 2.09 ± 0.21 (dry) ($p = 0.01$ for the APAR:SMC interaction term in Type II ANCOVA, based on linear regression without intercept). Furthermore, the monthly means of the SIF yield and θ_{5cm} show a nonlinear pattern (Figure 8b). Although the SIF-yield values have large errors, the smoothing curve for the entire 10-year data depicts a clear sigmoidal pattern, which is characteristic of wilting. There is no clear relationship between this SMC-associated change and Cab values.

The model calibration was conducted through a series of 44 10-year simulations. The best parameter set was found to be $V_{cmax} = 60$ (JJA) and 20 (other) $\mu\text{mol m}^{-2} \text{ s}^{-1}$, $g_{1M} = 4.61 \text{ kPa}^{1/2}$, $\theta_c = 16 \text{ vol}\%$, and $\theta_w = 10 \text{ vol}\%$

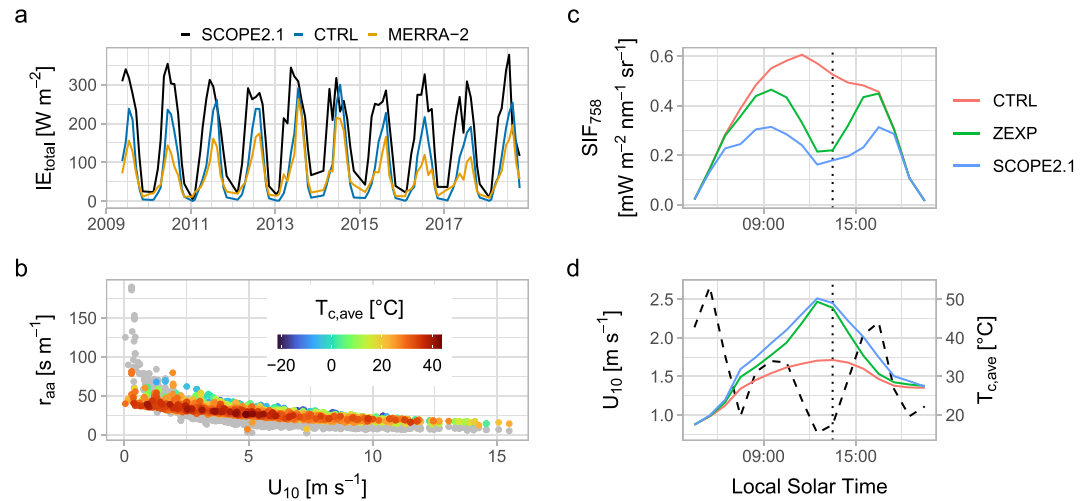


Figure 7. Model comparison results. (a) The latent heat of evapotranspiration IE_{total} at 13:30 local time (LT) throughout the study period. (b) Relationship between the above-canopy aerodynamic resistance r_{aa} and 10-m horizontal wind speed U_{10} at 13:30 LT. Gray and colored circles indicate the results from the original model (SCOPE2.1) and the control (CTRL) run, respectively. (c, d) Diurnal patterns of nadir-view SIF_{758} (c), U_{10} (dashed line in d), and average canopy temperature $T_{c,ave}$ (continuous lines in d) for the CTRL, ZEXP (zero thermal expansion) and SCOPE2.1 runs (see Section 4.2) on a calm summer day (23 July 2010). Vertical dotted lines indicate the overpass time of Greenhouse gases Observing Satellite (13:30 LT).

(RMSE = 0.754, mean bias = 0.004 $mW m^{-2} nm^{-1} sr^{-1}$ (JJA)). Notably, the modified model outperformed MERRA-2 in LST prediction when Aqua/MODIS was used as a reference. The mean bias was +1.16 K in the CAL run, +0.98 K in the CTRL run, and -4.4 K in MERRA-2. The evapotranspiration prediction was also improved, especially in the drought years (not shown), but the overall improvement was relatively minor: $r^2 = 0.70$ and 0.73 in the CTRL and CAL runs, respectively (Figure S7 in Supporting Information S1).

Figure 9a shows the differences in SIF_{758} between the CTRL and CAL runs. The improvement is obvious in 2016 and 2017, whereas the CAL run slightly underestimated SIF_{758} in the summers of 2009 and 2010. The underestimation in July 2009 was statistically significant ($p < 0.05$). The predicted GPP dynamics (Figure 9b) were similar to the LAI dynamics. The mean ratio of the around-noon (13:30 LT) GPP values in the CAL run to that in the CTRL run was 73% in all seasons and 91% in JJA, which indicates that SIF constrained GPP mostly

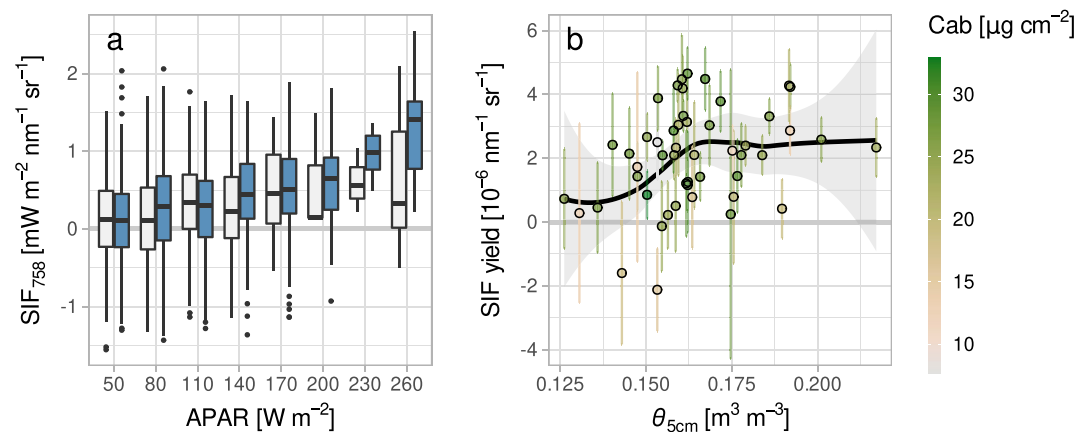


Figure 8. (a) Box-whisker plot of Greenhouse gases Observing Satellite (GOSAT) solar-induced chlorophyll fluorescence (SIF) against APAR binned at $30 W m^{-2}$ intervals. Blue and white boxes indicate the data with $\theta_{5cm} > 15.4$ and < 15.4 vol%, respectively. (b) Relationship between monthly means of GOSAT SIF yield and θ_{5cm} . Error bars indicate the standard error. The smoothing curve is the local regression; the smoothing span was determined by five-fold cross-validation that minimizes root mean square error within a range that produces a monotonic relationship of SIF yield and θ_{5cm} . The shading indicates the 95% confidence interval.

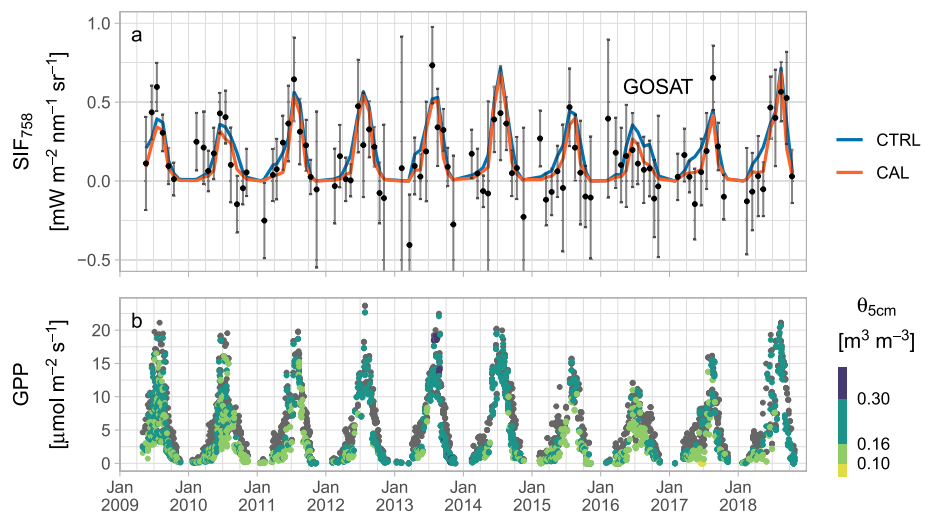


Figure 9. Comparison between uncalibrated (CTRL) and calibrated (CAL) run predictions for (a) SIF_{758} and (b) gross primary production at 13:30 local time. Circles and error bars in (a) indicate the monthly mean Greenhouse gases Observing Satellite solar-induced chlorophyll fluorescence (SIF) and its 90% confidence interval, respectively. Gray and colored circles in (b) indicate the CTRL and CAL runs, respectively.

through the tuning of phenology in V_{cmax} in ordinary years. However, in the drought years of 2016 and 2017, the ratio in JJA drops to 80% due to wilting (i.e., tuning $V_{cmax,app}$). Figure 10a shows a comparison of daily GPP between the CAL run and the MYD17 MODIS product. The CAL run tended to predict a larger GPP than the MODIS product; the ratio was 1.35 on average. The data are scattered around the line of the 1:1 relationship when $GPP < \sim 2.5 \text{ gC m}^{-2} \text{ d}^{-1}$, while in high-GPP cases, the CAL run predicted approximately 1.5 times the MODIS GPP. The wilting effect in the CAL run was evident, and the predicted GPP values sometimes became zero. Figures 10b and 10c show the comparison to two other GPP data sets (VPM and a machine-learning model). Our prediction showed larger GPP values than the two, on average, and a smaller value for the maximum. Among the four GPP data sets shown here, the machine-learning model showed the largest maximum value. Our prediction was most similar to the VPM GPP in the regression results (slope = 1.01, intercept = +0.43 $\text{gC m}^{-2} \text{ d}^{-1}$), while the highest r^2 was found in the comparison to the MODIS GPP.

6. Discussion

6.1. Comparison With Previous Studies and Key Findings

The CAL run predicted larger GPP values than did the MYD17 (Figure 10a), but they were within a reasonable range compared to other data sets (Figures 10b and 10c). Underestimation of grassland GPP in the MODIS

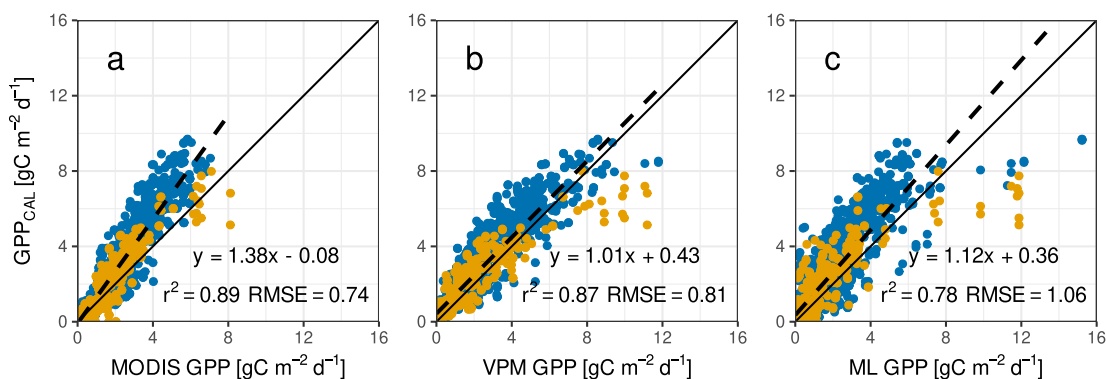


Figure 10. Relationships between simulated gross primary production (GPP) (CAL run, see text) and existing GPP data sets. (a) Moderate Resolution Imaging Spectroradiometer (MYD17 Collection 6), (b) VPM (Zhang et al., 2017), and (c) machine-learning (ML) regression using FLUXNET2015 (Zeng et al., 2020). The blue and orange circles indicate the data with $\theta_{5cm} > 15.4$ and < 15.4 vol%, respectively. The period for (b) is 2009–2017.

product is a known issue (Jiang & Ryu, 2016; Madani et al., 2014; Zhu et al., 2018). The highest r^2 value in comparison to MYD17 was probably due to the commonality in the meteorological data; we used MERRA-2 (GEOS-5 reanalysis), and MYD17 Collection 6 is also forced by GEOS-5. The CAL run's smaller GPP values than those of the VPM and the ML model in high-GPP cases are most likely due to wilting effects because the ML model neglects soil moisture (Zeng et al., 2020) and because the reflectance-based drought parameterization of the VPM using a water-absorption band is insufficient to quantify the wilting effect on GPP (Stocker et al., 2019). The CAL run likely overestimated GPP in low-GPP cases (especially evident in Figure 10c), which is attributable to our crude parameterization of V_{cmax} phenology (Section 4.2) and uncertain $J_{\text{max}}/V_{\text{cmax}}$ ratio. We used the default in MD12 ($J_{\text{max}}/V_{\text{cmax}} = 2.68$) (Leuning, 1997), but this ratio depends on growth conditions, for example, another meta-analysis by Medlyn et al. (2002) reported the typical ratio to be 1.67. A reduction in the $J_{\text{max}}/V_{\text{cmax}}$ ratio can reduce GPP without a change in SIF (Equation 4).

The CAL run predicted larger GPP values than MYD17, which is partly due to the increase in LAI and FVC (Figure 5). Note that the BIOME-BGC model used to calibrate MYD17 sets $V_{\text{cmax}} = 60 \mu\text{mol m}^{-2} \text{s}^{-1}$ for C3 grass, according to Rogers (2014). Therefore, the larger GPP values in our predictions are likely attributable to the differences in LAI, FVC, vertical V_{cmax} distribution, and stomatal conductance. The range of LAI increase from the a priori ($<1 \text{ m}^2 \text{ m}^{-2}$) falls within the product's uncertainty (Table 1; K. Yan et al., 2016), which is natural since we set the a priori uncertainty based on K. Yan et al. (2016). The increase in FVC ($<\sim 10\%$ pt) was not an expected result but is reasonable, as S. Huang and Siebert (2006) noted that MOD44B underestimated the FVC by 12.5% pt in the Mongolian Plateau compared with their on-site calibrated estimation.

A field measurement study for south Ural steppes ($51\text{--}57^\circ\text{N}$, precipitation $300\text{--}500 \text{ mm year}^{-1}$) reported that the summer peaks of C_{ab} were $30\text{--}45 \mu\text{g cm}^{-2}$ (Ivanov et al., 2013), which roughly agrees with our main retrieval results (Figure 5c) and is far larger than the results without considering FVC (Figure S5 in Supporting Information S1). This partly justifies our approach. On the other hand, we did not find field data of C_s for the Eurasian steppes. The brown pigment C_s has received less attention, although its potential effect on TOC SIF by changing the near-infrared f_{esc} is theoretically expected (Cui et al., 2020; Liu et al., 2019; van der Tol et al., 2019; Verrelst et al., 2015). Through a pure sensitivity analysis of the SCOPE model with nonreflecting soil assumption, Yang and van der Tol (2018) showed a strong sensitivity of near-infrared f_{esc} to LAI, whereas van der Tol et al. (2019) assumed moderate soil reflectance and showed a negligible LAI impact and that near-infrared f_{esc} highly depends on C_s and dry matter C_{dm} . Our inversion results indicate that the work of van der Tol et al. (2019) is more realistic (Figure 6) and show that the seasonal changes in the grassland f_{esc} are likely to be controlled by C_s but not C_{dm} (Figures 5 and 6; Figure S6 in Supporting Information S1).

The key findings of the present study can be summarized in three points. The first is observational evidence that GOSAT can detect the grassland wilting point (Figure 8). We found a nonlinear decrease in the GOSAT SIF when the surface SMC dropped below 15.4 vol%. The model-based analysis (i.e., estimated values of θ_c and θ_w) showed that the grassland GPP started to decrease at 16 vol% SMC and became almost zero at 10 vol% SMC. These values are close to the eddy-covariance results of S.-G. Li et al. (2005) conducted at a site near our study area; in that study, the net ecosystem exchange was classified according to surface SMC levels. The thresholds were >15 and <10 vol%, which agrees with our estimation within ~ 1 vol% ($\sim 0.01 \text{ m}^3 \text{ m}^{-3}$) SMC.

The second finding is the corroboration that the observed wilting point can be attributed to physiology (through apparent V_{cmax} as in Equation 5) after considering changes in canopy structure and leaf optical properties. Two model studies showed that satellite SIF could potentially be linked with root distribution (Forkel et al., 2019) or the wilting point for stomata (Qiu et al., 2018). However, chlorophyll reductions and turnover (C_s) effects on f_{esc} have not been evaluated, which significantly impact SIF (van der Tol et al., 2019) but have little impact on GPP. We retrieved these properties (Figures 5 and 6) and showed that (apparent) V_{cmax} tuning further improves SIF₇₅₈ prediction (Figure 9), which means that GOSAT SIF could provide an additional constraint on GPP that could not be derived from optical reflectance.

The third finding is the importance of surface energy balance and turbulent transport when evaluating SIF. As shown in Figure 7c, the grassland SIF predicted by SCOPE 2.1 was substantially lower than that of the CTRL run (150% error). Verma et al. (2017) also reported that SCOPE (v1.61, TB12) predicts substantially low SIF radiance compared with that retrieved by the Orbiting Carbon Observatory-2 (OCO-2) satellite in a C4 grassland ($\sim 200\%$ error in the worst case). Considering that the CAL run reproduced the GOSAT SIF₇₅₈ well (Figure 9a), we regard these discrepancies to be due to underestimation of the original SCOPE model and not due to bias in

GOSAT and OCO-2. The high canopy temperature predicted by SCOPE2.1 under unstable atmospheric conditions (Figures 7b and 7d) was expected from the nature of the built-in aerodynamic resistance scheme and a bug, that is, the local eddy diffusion assumption and fixed ρ_a . Therefore, we recommend that users of the SCOPE model avoid simulating low wind speed conditions without code modifications, especially when evaluating short vegetation.

6.2. Limitations and Future Implications

However, there are some uncertainties in photosynthesis-fluorescence schemes in model simulations. SIF-based retrievals of V_{cmax} attracted early attention, but up-to-date studies have reported their weak relationship (e.g., Koffi et al., 2015; Pacheco-Labrador et al., 2019; van der Tol et al., 2016; Verma et al., 2017; see also the review by Frankenberg & Berry, 2018). Figures 9 and 10 apparently contradict the up-to-date studies—the key difference was the use of the MD12 scheme here, which is more sensitive to physiology than the generally used TB12 (Verrelst et al., 2015). A leaf-scale model comparison study reported that MD12 outperforms TB12 (Mohammed et al., 2014), but their performance at a larger scale is unclear because MD12 is rarely used. Another problem is the uncertainty in the fraction of functional reaction center q_{Ls} that dominate the SIF predicted by MD12 (Verrelst et al., 2015). To our knowledge, the study of Porcar-Castell (2011) is the only report of the measurement of this parameter. Care needs to be taken that all results presented here are based on $q_{Ls} = 0.95$, which is adopted from the most unstressed condition in the study of Porcar-Castell (2011). The underestimation of SIF₇₅₈ in July 2009 (Figure 9) was potentially caused by reductions in q_{Ls} (see Equation 4), that is, drought-induced photoinhibition (Cornic & Massacci, 1996).

One important caveat about flux prediction is that our results support the ability of SIF to estimate the wilting point (as shown by the observation results in Figure 8) but do not strictly support its ability to estimate the maximum values of GPP and the transpiration rate. This is for the following three reasons. (a) The large uncertainty in the fluorescence parametrization that controls the maximum SIF values (q_{Ls} and J_{max}/V_{cmax} in MD12). (b) Although our GPP and evapotranspiration predictions were comparable to the existing data sets, this is partly due to the narrow search ranges of the parameter values (Table 2); the ranges were determined from the settings for the C3 grasslands in the established global models, except the wilting-point parameters θ_c and θ_w . This falls into a line of circular reasoning. (c) Improved agreements with MERRA-2 IE_{total} indirectly support the accuracy of transpiration and GPP, but they are insufficient. Individual validation for the calibrated parameters of the stomatal and soil surface resistance models is lacking here. The stomatal parameters were weakly constrained by SIF, which was confirmed by measurements (Magney et al., 2020; Wohlfahrt et al., 2018) and sensitivity analyses of SCOPE (Verrelst et al., 2015). However, even if field data are available, evapotranspiration partitioning is especially difficult for short vegetation because the established partition techniques for forests (e.g., sap flux sensors and multiheight eddy-covariance measurements) are not applicable. Evapotranspiration partitioning is an active research theme (Stoy et al., 2019).

Although C_s likely has nonnegligible impacts on grassland f_{esc} , further research is needed because our simulations (SCOPE and the RTMo inversion) assumed a homogeneous canopy; they did not separate the green and brown leaves or the canopy and litter. This limitation might overemphasize the contribution of C_s to f_{esc} , as shown in Figure 6. Recently, a multilayer heterogeneous canopy radiative transfer scheme was implemented in the forward prediction mode of SCOPE2.x (Yang et al., 2021), and Pacheco-Labrador et al. (2021) independently developed a new model composed of green and brown leaves based on SCOPE v1.73. However, they are not integrated and are not currently implemented in the RTMo inversion algorithm. Future studies using these new schemes with field-measured data sets of canopy compositions and SIF are warranted to understand the seasonal changes in f_{esc} . This line of research is worthwhile for grasses, crops, and marcescent trees (e.g., oak and beech).

The retrieved Cab values were scattered, as shown in Figure 5c. Although the SCOPE SIF saturates to changes in Cab when it exceeds $\sim 20 \mu\text{g cm}^{-2}$ (Koffi et al., 2015), the retrieved Cab values dropped below this threshold frequently in the summers of 2009 and 2010. Figure 9 shows that the predicted SIF₇₅₈ values in the CAL run moderately match those of GOSAT in 2010 but were underestimated in 2009; this may be caused by retrieval error in Cab . Due to this error, we cannot assert that the observed wilting pattern is definitively caused by physiology. However, this limitation results from the overlap of sensitive wavelengths between RTMo parameters (Figure 3). In other words, the limitation results from the optical nature of vegetation and soil. To increase the robustness of satellite-based GPP estimation, it is promising to combine SIF with thermal infrared radiation

(e.g., Pacheco-Labrador et al., 2019) and/or X-band microwaves. LST-based GPP estimation is preferable in its insensitivity to errors in *Cab* but requires fine tuning for aerodynamic resistance, SMC, and soil heat conduction; therefore, LST complementary works with SIF. We highlight that adequate modeling of surface energy balance and turbulent transport are fundamental to the application of this multiple-constraint approach and the evaluation of drought signals, as shown in this study.

Our method is highly based on radiative transfer and biophysical models, so its applicability to other regions is expected as long as the model assumptions are valid. The sun-sensor geometry significantly affects SIF radiance, and the 1D homogeneous canopy assumption in RTMo/SCOPE leads to serious bias in clumped canopies (e.g., Parazoo et al., 2020), so estimating a wilting point in a savanna with RTMo/SCOPE and the SIF from a polar-orbiting satellite is problematic. Another limitation is the precision of satellite SIF. We found it difficult to evaluate the GOSAT SIF yield around the center of the Mongolian Plateau (not shown), which has less precipitation and lower LAI; retrieval noise overwhelmed the weaker SIF signal. Therefore, the capability of GOSAT is likely limited to semiarid regions (precipitation $> \sim 400$ mm year⁻¹). In summary, our methodology in the present form using GOSAT and RTMo/SCOPE is expected to be valid in semiarid grasslands.

Data Availability Statement

The GOSAT TANSO-FTS L1B radiance data V202.202 and L4B atmospheric CO₂ concentration data V02.07 are available via the GOSAT Data Archive Service (<https://data2.gosat.nies.go.jp/>) after user registration. The MODIS Collection 6 data are available via the NASA Land Processes Distributed Active Archive Center (<https://lpdaac.usgs.gov/>) after user registration. The MODIS spectral response function is freely available at https://oceancolor.gsfc.nasa.gov/docs/rsr/rsr_tables/. The MERRA-2 reanalysis data are available via the Goddard Earth Sciences Data and Information Services Center (<https://disc.gsfc.nasa.gov/>) after user registration. The VPM and the machine-learning GPP data sets are available via figshare (<https://doi.org/10.6084/m9.figshare.c.3789814.v1>) and the NIES Global Environmental Database (<https://db.cger.nies.go.jp/ged/en/>), respectively. The global soil hydraulic property data set (Montzka et al., 2017) is distributed under the terms of the Creative Commons Attribution 3.0 via Pangea (<https://doi.org/10.1594/PANGAEA.870605>). The RTMo inversion algorithm version itc2020 and SCOPE Model v2.1 are distributed under GNU General Public License version 3 (GPLv3) and can be downloaded at https://github.com/Prikaziuk/retrieval_rtmo and <https://github.com/Christiaanvandertol/SCOPE>, respectively. The source code of the modified SCOPE model described in this paper is distributed under GPLv3 via Zenodo (<https://doi.org/10.5281/zenodo.7825064>).

Acknowledgments

This study was funded by the National Institute for Environmental Studies GOSAT and GOSAT-2 projects. SIF data were retrieved using the GOSAT-2 Research Computation Facility. We would like to thank Dr. Qinxue Wang at the National Institute for Environmental Studies and Prof. Jun Asanuma at the University of Tsukuba for providing information about field observations in Mongolia.

References

- Badr, H. S., Zaitchik, B. F., & Dezfuli, A. K. (2015). A tool for hierarchical climate regionalization. *Earth Science Informatics*, 8(4), 949–958. <https://doi.org/10.1007/s12145-015-0221-7>
- Baret, F., Hagolle, O., Geiger, B., Bicheron, P., Miras, B., Huc, M., et al. (2007). LAI, fAPAR and fCover CYCLOPES global products derived from VEGETATION. Part 1: Principles of the algorithm. *Remote Sensing of Environment*, 110(3), 275–286. <https://doi.org/10.1016/j.rse.2007.02.018>
- Bayat, B., van der Tol, C., & Verhoef, W. (2018). Integrating satellite optical and thermal infrared observations for improving daily ecosystem functioning estimations during a drought episode. *Remote Sensing of Environment*, 209, 375–394. <https://doi.org/10.1016/j.rse.2018.02.027>
- Bennett, W. B., Wang, J., & Bras, R. L. (2008). Estimation of global ground heat flux. *Journal of Hydrometeorology*, 9(4), 744–759. <https://doi.org/10.1175/2008JHM940.1>
- Biederman, J. A., Scott, R. L., Bell, T. W., Bowling, D. R., Dore, S., Garatuza-Payan, J., et al. (2017). CO₂ exchange and evapotranspiration across dryland ecosystems of southwestern North America. *Global Change Biology*, 23(10), 4204–4221. <https://doi.org/10.1111/gcb.13686>
- Bonan, G. (2015). *Ecological climatology*. Cambridge University Press. <https://doi.org/10.1017/cbo9781107339200>
- Brutsaert, W., & Sugita, M. (2008). Is Mongolia's groundwater increasing or decreasing? The case of the Kherlen River basin. *Hydrological Sciences Journal*, 53(6), 1221–1229. <https://doi.org/10.1623/hysj.53.6.1221>
- Cornic, G., & Massacci, A. (1996). Leaf photosynthesis under drought stress. In N. R. Baker (Ed.), *Photosynthesis and the environment. Advances in photosynthesis and respiration* (Vol. 5, pp. 347–366). Springer. https://doi.org/10.1007/0-306-48135-9_14
- Cui, T., Sun, R., Xiao, Z., Liang, Z., & Wang, J. (2020). Simulating spatially distributed solar-induced chlorophyll fluorescence using a BEPS-SCOPE coupling framework. *Agricultural and Forest Meteorology*, 295, 108169. <https://doi.org/10.1016/j.agrformet.2020.108169>
- Dayyoub, A. (2011). *Novel techniques for the remote sensing of photosynthetic processes*. Alma Digital Library (Doctoral dissertation). University of Bologna. <https://doi.org/10.6092/unibo/amsdottorato/3992>
- De Kauwe, M. G., Kala, J., Lin, Y. S., Pitman, A. J., Medlyn, B. E., Duursma, R. A., et al. (2015). A test of an optimal stomatal conductance scheme within the CABLE land surface model. *Geoscientific Model Development*, 8(2), 431–452. <https://doi.org/10.5194/gmd-8-431-2015>
- Dimiceli, C., Carroll, M., Sohlberg, R., Kim, D., Kelly, M., & Townshend, J. (2015). MOD44B MODIS/Terra vegetation continuous fields yearly L3 global 250m SIN grid V006 [Dataset]. NASA EOSDIS Land Processes DAAC. <https://doi.org/10.5067/MODIS/MOD44B.006>
- Doughy, R., Kurosu, T. P., Parazoo, N., Köhler, P., Wang, Y., Sun, Y., & Frankenberg, C. (2022). Global GOSAT, OCO-2, and OCO-3 solar-induced chlorophyll fluorescence datasets. *Earth System Science Data*, 14(4), 1513–1529. <https://doi.org/10.5194/essd-14-1513-2022>

- Farquhar, G. D., von Caemmerer, S., & Berry, J. A. (1980). A biochemical model of photosynthetic CO₂ assimilation in leaves of C3 species. *Planta*, 149(1), 78–90. <https://doi.org/10.1007/BF00386231>
- Fisher, J. B., Lee, B., Purdy, A. J., Halverson, G. H., Dohlen, M. B., Cawse-Nicholson, K., et al. (2020). ECOSTRESS: NASA's next generation mission to measure evapotranspiration from the International space station. *Water Resources Research*, 56(4), e2019WR026058. <https://doi.org/10.1029/2019WR026058>
- Flexas, J., Barbour, M. M., Brendel, O., Cabrera, H. M., Carriqui, M., Díaz-Espejo, A., et al. (2012). Mesophyll diffusion conductance to CO₂: An unappreciated central player in photosynthesis. *Plant Science*, 193–194, 70–84. <https://doi.org/10.1016/j.plantsci.2012.05.009>
- Forkel, M., Druke, M., Thurner, M., Dorigo, W., Schaphoff, S., Thonicke, K., et al. (2019). Constraining modelled global vegetation dynamics and carbon turnover using multiple satellite observations. *Scientific Reports*, 9(1), 18757. <https://doi.org/10.1038/s41598-019-55187-7>
- Frankenberg, C., & Berry, J. (2018). Solar induced chlorophyll fluorescence: Origins, relation to photosynthesis and retrieval. In S. Liang (Ed.), *Comprehensive remote sensing* (Vol. 3, pp. 143–162). Elsevier. <https://doi.org/10.1016/B978-0-12-409548-9.10632-3>
- Friedl, M., & Sulla-Menasse, D. (2019). MCD12Q1 MODIS/Terra+Aqua land cover Type yearly L3 global 500 m SIN grid V006 [Dataset]. NASA EOSDIS Land Processes DAAC. <https://doi.org/10.5067/MODIS/MCD12Q1.006>
- Fuster, B., Sánchez-Zapero, J., Camacho, F., García-Santos, V., Verger, A., Lacaze, R., et al. (2020). Quality assessment of PROBA-V LAI, fAPAR and fCOVER collection 300 m products of Copernicus global land service. *Remote Sensing*, 12(6), 1017. <https://doi.org/10.3390/rs12061017>
- Gelaro, R., McCarty, W., Suárez, M. J., Todling, R., Molod, A., Takacs, L., et al. (2017). The modern-era retrospective analysis for research and applications, version 2 (MERRA-2). *Journal of Climate*, 30(14), 5419–5454. <https://doi.org/10.1175/JCLI-D-16-0758.1>
- Gruber, A., Scanlon, T., Van Der Schalie, R., Wagner, W., & Dorigo, W. (2019). Evolution of the ESA CCI Soil Moisture climate data records and their underlying merging methodology. *Earth System Science Data*, 11(2), 717–739. <https://doi.org/10.5194/essd-11-717-2019>
- Hornberger, G. M., Wiberg, P. L., Raffensperger, J. P., & D'Odorico, P. (2014). *Elements of physical hydrology*. Johns Hopkins University Press.
- Huang, J., Li, Y., Fu, C., Chen, F., Fu, Q., Dai, A., et al. (2017). Dryland climate change: Recent progress and challenges. *Reviews of Geophysics*, 55(3), 719–778. <https://doi.org/10.1002/2016RG000550>
- Huang, S., & Siegert, F. (2006). Land cover classification optimized to detect areas at risk of desertification in North China based on SPOT VEGETATION imagery. *Journal of Arid Environments*, 67(2), 308–327. <https://doi.org/10.1016/j.jaridenv.2006.02.016>
- Ivanov, L. A., Ivanova, L. A., Ronzhina, D. A., & Yudina, P. K. (2013). Changes in the chlorophyll and carotenoid contents in the leaves of steppe plants along a latitudinal gradient in South Ural. *Russian Journal of Plant Physiology*, 60(6), 812–820. <https://doi.org/10.1134/S1021443713050075>
- Jacquemoud, S., & Baret, F. (1990). PROSPECT: A model of leaf optical properties spectra. *Remote Sensing of Environment*, 34(2), 75–91. [https://doi.org/10.1016/0034-4257\(90\)90100-Z](https://doi.org/10.1016/0034-4257(90)90100-Z)
- Jiang, C., & Ryu, Y. (2016). Multi-scale evaluation of global gross primary productivity and evapotranspiration products derived from Breathing Earth System Simulator (BESS). *Remote Sensing of Environment*, 186, 528–547. <https://doi.org/10.1016/j.rse.2016.08.030>
- Jonard, F., De Cannière, S., Brüggemann, N., Gentile, P., Short Gianotti, D. J., Lobet, G., et al. (2020). Value of sun-induced chlorophyll fluorescence for quantifying hydrological states and fluxes: Current status and challenges. *Agricultural and Forest Meteorology*, 291, 108088. <https://doi.org/10.1016/j.agrformet.2020.108088>
- Kattge, J., & Knorr, W. (2007). Temperature acclimation in a biochemical model of photosynthesis: A reanalysis of data from 36 species. *Plant, Cell and Environment*, 30(9), 1176–1190. <https://doi.org/10.1111/j.1365-3040.2007.01690.x>
- Kobayashi, S., Ota, Y., Harada, Y., Ebata, A., Moriya, M., Onoda, H., et al. (2015). The JRA-55 reanalysis: General specifications and basic characteristics. *Journal of the Meteorological Society of Japan*, 93(1), 5–48. <https://doi.org/10.2151/jmsj.2015-001>
- Koffi, E. N., Rayner, P. J., Norton, A. J., Frankenberg, C., & Scholze, M. (2015). Investigating the usefulness of satellite-derived fluorescence data in inferring gross primary productivity within the carbon cycle data assimilation system. *Biogeosciences*, 12(13), 4067–4084. <https://doi.org/10.5194/bg-12-4067-2015>
- Lawrence, D., Fisher, R., Koven, C., Oleson, K., Swenson, S., Vertenstein, M., et al. (2020). *CLM5 documentation*. National Center for Atmospheric Research. Retrieved from https://www.cesm.ucar.edu/models/cesm2/land/CLM50_Tech_Note.pdf
- Lee, E.-H., & Sohn, B.-J. (2011). Recent increasing trend in dust frequency over Mongolia and Inner Mongolia regions and its association with climate and surface condition change. *Atmospheric Environment*, 45(27), 4611–4616. <https://doi.org/10.1016/j.atmosenv.2011.05.065>
- Leuning, R. (1997). Scaling to a common temperature improves the correlation between the photosynthesis parameters J_{max} and V_{cmax} . *Journal of Experimental Botany*, 48(2), 345–347. <https://doi.org/10.1093/jxb/48.2.345>
- Li, H., Ye, A., Zhang, Y., & Zhao, W. (2021). Intercomparison and evaluation of multisource soil moisture products in China. *Earth and Space Science*, 8(10), e2021EA001845. <https://doi.org/10.1029/2021EA001845>
- Li, S.-G., Asanuma, J., Eugster, W., Kotani, A., Liu, J.-J., Urano, T., et al. (2005). Net ecosystem carbon dioxide exchange over grazed steppe in central Mongolia. *Global Change Biology*, 11(11), 1941–1955. <https://doi.org/10.1111/j.1365-2486.2005.01047.x>
- Liu, W., Atherton, J., Möttus, M., Gastellu-Etchegorry, J.-P., Malenovsky, Z., Raunonen, P., et al. (2019). Simulating solar-induced chlorophyll fluorescence in a boreal forest stand reconstructed from terrestrial laser scanning measurements. *Remote Sensing of Environment*, 232, 111274. <https://doi.org/10.1016/j.rse.2019.111274>
- Lloyd, J., Patiño, S., Paiva, R. Q., Nardoto, G. B., Quesada, C. A., Santos, A. J. B., et al. (2010). Optimisation of photosynthetic carbon gain and within-canopy gradients of associated foliar traits for Amazon forest trees. *Biogeosciences*, 7(6), 1833–1859. <https://doi.org/10.5194/bg-7-1833-2010>
- Lyapustin, A., & Wang, Y. (2018). MCD19A1 MODIS/Terra+Aqua land surface BRDF daily L2G global 500 m and 1km SIN grid V006 [Dataset]. NASA EOS-DIS Land Processes DAAC. <https://doi.org/10.5067/MODIS/MCD19A1.006>
- Lyapustin, A., Wang, Y., Xiong, X., Meister, G., Platnick, S., Levy, R., et al. (2014). Scientific impact of MODIS C5 calibration degradation and C6+ improvements. *Atmospheric Measurement Techniques*, 7(12), 4353–4365. <https://doi.org/10.5194/amt-7-4353-2014>
- Madani, N., Kimball, J. S., Affleck, D. L. R., Kattge, J., Graham, J., Van Bodegom, P. M., et al. (2014). Improving ecosystem productivity modeling through spatially explicit estimation of optimal light use efficiency. *Journal of Geophysical Research: Biogeosciences*, 119(9), 1755–1769. <https://doi.org/10.1002/2014JG002709>
- Magney, T. S., Barnes, M. L., & Yang, X. (2020). On the covariation of chlorophyll fluorescence and photosynthesis across scales. *Geophysical Research Letters*, 47(23), e2020GL091098. <https://doi.org/10.1029/2020GL091098>
- Martens, B., Miralles, D. G., Lievens, H., Van Der Schalie, R., De Jeu, R. A., Fernández-Prieto, D., et al. (2017). GLEAM v3: Satellite-based land evaporation and root-zone soil moisture. *Geoscientific Model Development*, 10(5), 1903–1925. <https://doi.org/10.5194/gmd-10-1903-2017>
- Medlyn, B. E., Dreyer, E., Ellsworth, D., Forstreuter, M., Harley, P. C., Kirschbaum, M. U. F., et al. (2002). Temperature response of parameters of a biochemically based model of photosynthesis. II. A review of experimental data. *Plant, Cell and Environment*, 25(9), 1167–1179. <https://doi.org/10.1046/j.1365-3040.2002.00891.x>

- Medlyn, B. E., Duursma, R. A., Eamus, D., Ellsworth, D. S., Prentice, I. C., Barton, C. V. M., et al. (2011). Reconciling the optimal and empirical approaches to modelling stomatal conductance. *Global Change Biology*, 17(6), 2134–2144. <https://doi.org/10.1111/j.1365-2486.2010.02375.x>
- Mohammed, G. H., Goulas, Y., Magnani, F., Moreno, J., Julie, O., Rascher, U., et al. (2014). *FLEX/Sentinel 3 tandem mission photosynthesis study—FINAL REPORT*. P and M Technologies. Retrieved from http://www.flex-photosyn.ca/PS_FinalReport.htm
- Montzka, C., Herbst, M., Weihermüller, L., Verhoef, A., & Vereecken, H. (2017). A global data set of soil hydraulic properties and sub-grid variability of soil water retention and hydraulic conductivity curves. *Earth System Science Data*, 9(2), 529–543. <https://doi.org/10.5194/essd-9-529-2017>
- Myneni, R., Knyazikhin, Y., & Park, T. (2015). MCD15A2H MODIS/Terra+Aqua leaf area index/FPAR 8-day L4 global 500 m SIN grid V006 [Dataset]. NASA EOSDIS Land Processes DAAC. <https://doi.org/10.5067/MODIS/MCD15A2H.006>
- Nandintsetseg, B., Shinoda, M., Du, C., & Munkhjargal, E. (2018). Cold-season disasters on the Eurasian steppes: Climate-driven or man-made. *Scientific Reports*, 8(1), 14769. <https://doi.org/10.1038/s41598-018-33046-1>
- Oshio, H., Yoshida, Y., & Matsunaga, T. (2019). On the zero-level offset in the GOSAT TANSO-FTS O2 A band and the quality of solar-induced chlorophyll fluorescence (SIF): Comparison of SIF between GOSAT and OCO-2. *Atmospheric Measurement Techniques*, 12(12), 6721–6735. <https://doi.org/10.5194/amt-12-6721-2019>
- Pacheco-Labrador, J., El-Madany, T. S., van der Tol, C., Martin, M. P., Gonzalez-Cascon, R., Perez-Priego, O., et al. (2021). senSCOPE: Modeling mixed canopies combining green and Brown senesced leaves. Evaluation in a Mediterranean Grassland. *Remote Sensing of Environment*, 257, 112352. <https://doi.org/10.1016/j.rse.2021.112352>
- Pacheco-Labrador, J., Perez-Priego, O., El-Madany, T. S., Julitta, T., Rossini, M., Guan, J., et al. (2019). Multiple-constraint inversion of SCOPE. Evaluating the potential of GPP and SIF for the retrieval of plant functional traits. *Remote Sensing of Environment*, 234, 111362. <https://doi.org/10.1016/j.rse.2019.111362>
- Parazoo, N. C., Magney, T., Norton, A., Raczka, B., Bacour, C., Maignan, F., et al. (2020). Wide discrepancies in the magnitude and direction of modeled solar-induced chlorophyll fluorescence in response to light conditions. *Biogeosciences*, 17(13), 3733–3755. <https://doi.org/10.5194/bg-17-3733-2020>
- Paschalis, A., Katul, G. G., Faticchi, S., Palmroth, S., & Way, D. (2017). On the variability of the ecosystem response to elevated atmospheric CO₂ across spatial and temporal scales at the Duke Forest FACE experiment. *Agricultural and Forest Meteorology*, 232, 367–383. <https://doi.org/10.1016/j.agrformet.2016.09.003>
- Porcar-Castell, A. (2011). A high-resolution portrait of the annual dynamics of photochemical and non-photochemical quenching in needles of *Pinus sylvestris*. *Physiologia Plantarum*, 143(2), 139–153. <https://doi.org/10.1111/j.1399-3054.2011.01488.x>
- Qiu, B., Xue, Y., Fisher, J. B., Guo, W., Berry, J. A., & Zhang, Y. (2018). Satellite chlorophyll fluorescence and soil moisture observations lead to advances in the predictive understanding of global terrestrial coupled carbon-water cycles. *Global Biogeochemical Cycles*, 32(3), 360–375. <https://doi.org/10.1002/2017GB005744>
- Rawls, W. J., Ahuja, L. R., Brakensiek, D. L., & Shirmohammadi, A. (1992). Infiltration and soil water movement. In D. R. Maidment (Ed.), *Handbook of hydrology* (pp. 5.1–5.51). McGraw-Hill.
- Reichle, R. H., Draper, C. S., Liu, Q., Giroto, M., Mahanama, S. P. P., Koster, R. D., & De Lannoy, G. J. M. (2017). Assessment of MERRA-2 land surface hydrology estimates. *Journal of Climate*, 30(8), 2937–2960. <https://doi.org/10.1175/JCLI-D-16-0720.1>
- Rodgers, C. D. (2000). *Inverse methods for atmospheric sounding: Theory and practice*. World Scientific. <https://doi.org/10.1142/3171>
- Rogers, A. (2014). The use and misuse of $V_{c,max}$ in Earth System Models. *Photosynthesis Research*, 119(1–2), 15–29. <https://doi.org/10.1007/s11120-013-9818-1>
- Rogers, A., Medlyn, B. E., Dukes, J. S., Bonan, G., von Caemmerer, S., Dietze, M. C., et al. (2017). A roadmap for improving the representation of photosynthesis in Earth system models. *New Phytologist*, 213(1), 22–42. <https://doi.org/10.1111/nph.14283>
- Running, S. W., Mu, Q., & Zhao, M. (2015). MYD17A2H MODIS/Aqua gross primary productivity 8-day L4 global 500 m SIN grid V006. [Dataset]. NASA EOSDIS Land Processes DAAC. <https://doi.org/10.5067/MODIS/MYD17A2H.006>
- Sims, D. A., & Gamon, J. A. (2002). Relationships between leaf pigment content and spectral reflectance across a wide range of species, leaf structures and developmental stages. *Remote Sensing of Environment*, 81(2–3), 337–354. [https://doi.org/10.1016/S0034-4257\(02\)00010-X](https://doi.org/10.1016/S0034-4257(02)00010-X)
- Sperry, J. S., & Love, D. M. (2015). What plant hydraulics can tell us about responses to climate-change droughts. *New Phytologist*, 207(1), 14–27. <https://doi.org/10.1111/nph.13354>
- Stocker, B. D., Zscheischler, J., Keenan, T. F., Prentice, I. C., Seneviratne, S. I., & Peñuelas, J. (2019). Drought impacts on terrestrial primary production underestimated by satellite monitoring. *Nature Geoscience*, 12(4), 264–270. <https://doi.org/10.1038/s41561-019-0318-6>
- Stoy, P. C., El-Madany, T. S., Fisher, J. B., Gentine, P., Gerken, T., Good, S. P., et al. (2019). Reviews and syntheses: Turning the challenges of partitioning ecosystem evaporation and transpiration into opportunities. *Biogeosciences*, 16(19), 3747–3775. <https://doi.org/10.5194/bg-16-3747-2019>
- Stull, R. B. (1988). *An introduction to boundary layer meteorology*. Springer. <https://doi.org/10.1007/978-94-009-3027-8>
- Tardieu, F., Simonneau, T., & Parent, B. (2015). Modelling the coordination of the controls of stomatal aperture, transpiration, leaf growth, and abscisic acid: Update and extension of the Tardieu-Davies model. *Journal of Experimental Botany*, 66(8), 2227–2237. <https://doi.org/10.1093/jxb/erv039>
- Thum, T., Zaehle, S., Köhler, P., Aalto, T., Aurela, M., Guanter, L., et al. (2017). Modelling sun-induced fluorescence and photosynthesis with a land surface model at local and regional scales in northern Europe. *Biogeosciences*, 14(7), 1969–1984. <https://doi.org/10.5194/bg-14-1969-2017>
- Trugman, A. T., Medvigy, D., Mankin, J. S., & Anderegg, W. R. L. (2018). Soil moisture stress as a major driver of carbon cycle uncertainty. *Geophysical Research Letters*, 45(13), 6495–6503. <https://doi.org/10.1029/2018GL078131>
- van der Tol, C., Rossini, M., Cogliati, S., Verhoef, W., Colombo, R., Rascher, U., & Mohammed, G. (2016). A model and measurement comparison of diurnal cycles of sun-induced chlorophyll fluorescence of crops. *Remote Sensing of Environment*, 186, 663–677. <https://doi.org/10.1016/j.rse.2016.09.021>
- van der Tol, C., Verhoef, W., Timmermans, J., Verhoef, A., & Su, Z. (2009). An integrated model of soil-canopy spectral radiances, photosynthesis, fluorescence, temperature and energy balance. *Biogeosciences*, 6(12), 3109–3129. <https://doi.org/10.5194/bg-6-3109-2009>
- van der Tol, C., Vilfan, N., Dauwe, D., Cendrero-Mateo, M. P., & Yang, P. (2019). The scattering and re-absorption of red and near-infrared chlorophyll fluorescence in the models Fluspect and SCOPE. *Remote Sensing of Environment*, 232, 111292. <https://doi.org/10.1016/j.rse.2019.111292>
- Verhoef, A., & Egea, G. (2014). Modeling plant transpiration under limited soil water: Comparison of different plant and soil hydraulic parameterizations and preliminary implications for their use in land surface models. *Agricultural and Forest Meteorology*, 191, 22–32. <https://doi.org/10.1016/j.agrformet.2014.02.009>

- Verhoef, W. (1998). *Theory of radiative transfer models applied in optical remote sensing of vegetation canopies* (Doctoral dissertation). Wageningen University and Research Library, Wageningen Agricultural University. Retrieved from <https://library.wur.nl/WebQuery/wurpubs/43047>
- Verhoef, W., van der Tol, C., & Middleton, E. M. (2018). Hyperspectral radiative transfer modeling to explore the combined retrieval of biophysical parameters and canopy fluorescence from FLEX—Sentinel-3 tandem mission multi-sensor data. *Remote Sensing of Environment*, *204*, 942–963. <https://doi.org/10.1016/j.rse.2017.08.006>
- Verma, M., Schimel, D., Evans, B., Frankenberg, C., Beringer, J., Drewry, D. T., et al. (2017). Effect of environmental conditions on the relationship between solar-induced fluorescence and gross primary productivity at an OzFlux grassland site. *Journal of Geophysical Research: Biogeosciences*, *122*(3), 716–733. <https://doi.org/10.1002/2016JG003580>
- Verrelst, J., Rivera, J. P., van der Tol, C., Magnani, F., Mohammed, G., & Moreno, J. (2015). Global sensitivity analysis of the SCOPE model: What drives simulated canopy-leaving sun-induced fluorescence? *Remote Sensing of Environment*, *166*, 8–21. <https://doi.org/10.1016/j.rse.2015.06.002>
- Wallece, J. S., & Verhoef, A. (2000). Modelling interactions in mixed-plant communities: Light, water and carbon dioxide. In B. Marshall & J. A. Roberts (Eds.), *Leaf development and canopy growth* (pp. 204–250). Blackwell.
- Wan, Z., Hook, S., & Hulley, G. (2015). MYD11A1 MODIS/Aqua land surface temperature/emissivity daily L3 global 1 km SIN grid V006 [Dataset]. NASA EOSDIS Land Processes DAAC. Retrieved from <https://ladsweb.modaps.eosdis.nasa.gov/missions-and-measurements/products/MYD11A1>
- Wei, J., Dirmeyer, P. A., Wissler, D., Bosilovich, M. G., & Mocko, D. M. (2013). Where does the irrigation water go? An estimate of the contribution of irrigation to precipitation using MERRA. *Journal of Hydrometeorology*, *14*(1), 275–289. <https://doi.org/10.1175/JHM-D-12-079.1>
- Weiss, M., & Baret, F. (2016). *S2ToolBox level 2 products: LAI, FAPAR, FCOVER version 1.1*. Institut National de la recherche agronomique. Retrieved from https://step.esa.int/docs/extra/ATBD_S2ToolBox_L2B_V1.1.pdf
- Weiss, M., Baret, F., Garrigues, S., & Lacaze, R. (2007). LAI and FAPAR CYCLOPES global products derived from VEGETATION. Part 2: Validation and comparison with MODIS collection 4 products. *Remote Sensing of Environment*, *110*(3), 317–331. <https://doi.org/10.1016/j.rse.2007.03.001>
- Wohlfahrt, G., Gerdel, K., Migliavacca, M., Rotenberg, E., Tatarinov, F., Müller, J., et al. (2018). Sun-induced fluorescence and gross primary productivity during a heat wave. *Scientific Reports*, *8*(1), 14169. <https://doi.org/10.1038/s41598-018-32602-z>
- Xu, Z., Fan, K., & Wang, H. (2015). Decadal variation of summer precipitation over China and associated atmospheric circulation after the late 1990s. *Journal of Climate*, *28*(10), 4086–4106. <https://doi.org/10.1175/JCLI-D-14-00464.1>
- Yan, K., Park, T., Yan, G., Liu, Z., Yang, B., Chen, C., et al. (2016). Evaluation of MODIS LAI/FPAR product collection 6. Part 2: Validation and intercomparison. *Remote Sensing*, *8*(6), 460. <https://doi.org/10.3390/rs8060460>
- Yan, Y., Yan, R., Chen, J., Xin, X., Eldridge, D. J., Shao, C., et al. (2018). Grazing modulates soil temperature and moisture in a Eurasian steppe. *Agricultural and Forest Meteorology*, *262*, 157–165. <https://doi.org/10.1016/j.agrformet.2018.07.011>
- Yang, P., Prikaziuk, E., Verhoef, W., & van der Tol, C. (2021). Scope 2.0: A model to simulate vegetated land surface fluxes and satellite signals. *Geoscientific Model Development*, *14*(7), 4697–4712. <https://doi.org/10.5194/gmd-14-4697-2021>
- Yang, P., & van der Tol, C. (2018). Linking canopy scattering of far-red sun-induced chlorophyll fluorescence with reflectance. *Remote Sensing of Environment*, *209*, 456–467. <https://doi.org/10.1016/j.rse.2018.02.029>
- Yang, P., van der Tol, C., Yin, T., & Verhoef, W. (2020). The SPART model: A soil-plant-atmosphere radiative transfer model for satellite measurements in the solar spectrum. *Remote Sensing of Environment*, *247*, 111870. <https://doi.org/10.1016/j.rse.2020.111870>
- Zeng, J., Matsunaga, T., Tan, Z. H., Saigusa, N., Shirai, T., Tang, Y., et al. (2020). Global terrestrial carbon fluxes of 1999–2019 estimated by upscaling eddy covariance data with a random forest. *Scientific Data*, *7*(1), 313. <https://doi.org/10.1038/s41597-020-00653-5>
- Zhang, Y., Xiao, X., Wu, X., Zhou, S., Zhang, G., Qin, Y., & Dong, J. (2017). A global moderate resolution dataset of gross primary production of vegetation for 2000–2016. *Scientific Data*, *4*(1), 170165. <https://doi.org/10.1038/sdata.2017.165>
- Zhou, S., Duursma, R. A., Medlyn, B. E., Kelly, J. W. G., & Prentice, I. C. (2013). How should we model plant responses to drought? An analysis of stomatal and non-stomatal responses to water stress. *Agricultural and Forest Meteorology*, *182–183*, 204–214. <https://doi.org/10.1016/j.agrformet.2013.05.009>
- Zhu, X., Pei, Y., Zheng, Z., Dong, J., Zhang, Y., Wang, J., et al. (2018). Underestimates of grassland gross primary production in MODIS standard products. *Remote Sensing*, *10*(11), 1771. <https://doi.org/10.3390/rs10111771>

References From the Supporting Information

- Aarts, E., Verhage, M., Veenfliet, J. V., Dolan, C. V., & Van Der Sluis, S. (2014). A solution to dependency: Using multilevel analysis to accommodate nested data. *Nature Neuroscience*, *17*(4), 491–496. <https://doi.org/10.1038/nn.3648>
- Best, M. J., Pryor, M., Clark, D. B., Rooney, G. G., Essery, R. L. H., Ménard, C. B., et al. (2011). The joint UK Land Environment Simulator (JULES), model description—Part 1: Energy and water fluxes. *Geoscientific Model Development*, *4*(3), 677–699. <https://doi.org/10.5194/gmd-4-677-2011>
- Dutta, D., Schimel, D. S., Sun, Y., Van Der Tol, C., & Frankenberg, C. (2019). Optimal inverse estimation of ecosystem parameters from observations of carbon and energy fluxes. *Biogeosciences*, *16*(1), 77–103. <https://doi.org/10.5194/bg-16-77-2019>
- Jarvis, P. G., & Mcnaughton, K. G. (1986). Stomatal control of transpiration: Scaling up from leaf to region. In A. MacFadyen & E. D. Ford (Eds.), *Advances in ecological research* (Vol. 15, pp. 1–49). Elsevier. [https://doi.org/10.1016/S0065-2504\(08\)60119-1](https://doi.org/10.1016/S0065-2504(08)60119-1)
- Kuze, A., Suto, H., Shiomi, K., Kawakami, S., Tanaka, M., Ueda, Y., et al. (2016). Update on GOSAT TANSO-FTS performance, operations, and data products after more than 6 years in space. *Atmospheric Measurement Techniques*, *9*(6), 2445–2461. <https://doi.org/10.5194/amt-9-2445-2016>
- Sellers, P. J., Randall, D. A., Collatz, G. J., Berry, J. A., Field, C. B., Dazlich, D. A., et al. (1996). A revised land surface parameterization (SiB2) for atmospheric GCMs. Part I: Model formulation. *Journal of Climate*, *9*(4), 676–705. [https://doi.org/10.1175/1520-0442\(1996\)009<0676:ARLSPF>2.0.CO;2](https://doi.org/10.1175/1520-0442(1996)009<0676:ARLSPF>2.0.CO;2)
- Vermote, E. F., & Vermeulen, A. (1999). Atmospheric correction algorithm: Spectral reflectances (MOD09) Version 4.0 (NASA contract NASS-96062). Retrieved from https://modis.gsfc.nasa.gov/data/atbd/atbd_mod08.pdf